



A micro–macro investigation of the capillary strengthening effect in wet granular materials

Ji-Peng Wang^{1,2} · Xia Li^{3,4} · Hai-Sui Yu⁵

Received: 7 December 2016 / Accepted: 11 December 2017 / Published online: 20 December 2017
© Springer-Verlag GmbH Germany, part of Springer Nature 2017

Abstract

Wet granular materials are three-dimensionally simulated by the discrete element method with water bridges incorporated between particles. The water bridges are simplified as toroidal shapes, and the matric suction is constantly maintained in the material. A comparison with experimental tests in the literature indicates that the toroidal shape approximation may be one of the best choices with high practicability and decent accuracy. Mechanical behaviours of wet granular materials are studied by triaxial tests. Effects of particle size distributions and void ratios are investigated systematically in this study. The hydraulic limit of the pendular state is also discussed. It gives the capillary cohesion function which is not only determined by the degree of saturation but also positively correlated to relative density and particle size polydispersity and inversely proportional to mean particle size. Furthermore, the capillary strengthening effect is also analysed microscopically in aid of the Stress–Force–Fabric relationship, mainly in fabric anisotropy, coordination number and stress transmission pattern, which revealed the micro-mechanisms of the additional effective stress induced by capillary effect.

Keywords Capillary cohesion · DEM · Micro-mechanics · Particle size distribution · Unsaturated granular materials · Water bridge

1 Introduction

Dry granular materials have specific repose angles, however, by adding a small amount of water the materials are strengthened and a sand castle can stand [19, 46]. Further increase in water content may lead the sand castle to collapse. Theoretically, it can be explained that the change of moisture content in this water–air–solid mixture alters the suction (defined as the pressure difference between air and water phases) and increased the ‘effective stress’ for the partially saturated cases [1, 2, 33]. Microscopically, with the increase in water content, the morphology of the water phase in a granular media can be categorised as the pendular state, the funicular state and the capillary state [38, 40] as illustrated in Fig. 1. In the pendular state, usually less than 10% of degree of saturation, isolated water bridges are formed between particles and the attractive forces acting through the water bridges raise the material cohesion significantly. With the increase in water content, the water bridges begin to coalesce with each other to form liquid clusters. In this state, it is argued that the capillary force is slightly reduced and the rupture distance

✉ Ji-Peng Wang
Ji-Peng.Wang@outlook.com

Xia Li
xia.li@seu.edu.cn

Hai-Sui Yu
h.yu@leeds.ac.uk

¹ Nottingham Centre for Geomechanics, University of Nottingham, University Park, Nottingham NG7 2RD, UK

² Present Address: Building Architecture and Town Planning Department (BATir), Université Libre de Bruxelles, Avenue F.D. Roosevelt 50, CP 194/2, 1050 Brussels, Belgium

³ School of Civil Engineering, Southeast University, Nanjing 210018, China

⁴ Key Laboratory of Concrete and Prestressed Concrete Structures of the Ministry of Education, Southeast University, Nanjing 210018, China

⁵ School of Civil Engineering, Faculty of Engineering, University of Leeds, Leeds LS2 9JT, UK

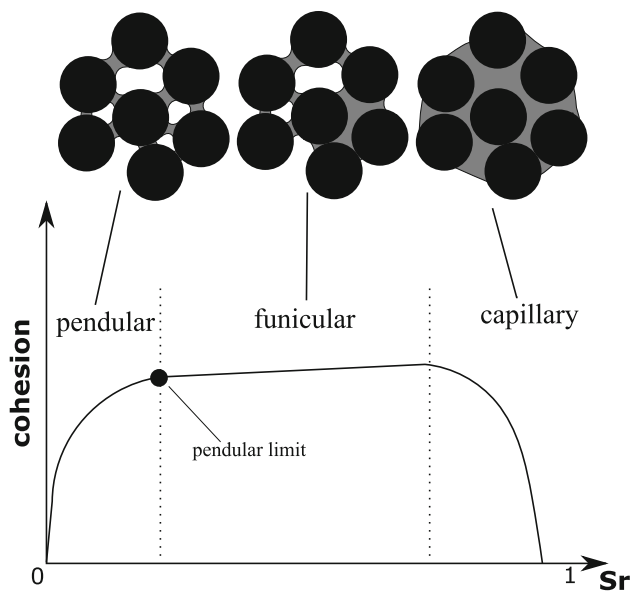


Fig. 1 Different saturation states and cohesion of wet granular materials

may be extended [50, 60]; thus, the combination effect from capillary force and rupture distance lead the capillary cohesion to be about constant [46]. When the material reached the capillary state, as the material is nearly saturated with only small air bubbles, the material cohesion is also reduced to about zero. Therefore, to discuss the limit of the pendular state and the water bridge effect could explain the capillary strengthening effect and the capillary cohesion of granular materials.

The capillary bridge effect between two idealised grains (spheres) has been well studied in the literature. The initial work is done by Haines and Fisher [8, 15, 16] in which the liquid bridge between two mono-sized discs in contact is simplified as toroidal shape (the profile of the water bridge is in a circle). Later, Rose [44] addressed the effect from separation distance and water–air–solid contact angle on liquid volumes. Experimental tests done by Mason and Clark [35] measured the capillary force and rupture distance of the liquid bridge between two spheres. The 'gorge method' to calculate the capillary force is then expressed as the sum of pressure and surface tension acting on the neck section by Hotta [20]. Following the pioneer's work and by introducing the Young–Laplace equation, the capillary force of a capillary bridge with a constant volume is solved [28, 51]. This solution is also expressed in a constant suction condition [48] for further numerical implementations. Besides the solutions from the Young–Laplace equation, the toroidal approximation is still employed in the recent research by providing reasonable results on both capillary force and liquid volume by comparing with other solutions [12, 17].

The discrete element method (DEM) is firstly proposed for the micro-mechanical study of granular materials [5]. By implementing the water bridge solutions between spherical grains, wet granular materials are simulated and studied by DEM method in the recent two decades. It is firstly simulated in two-dimensional conditions [10, 21, 29] and then extended to three-dimensional spaces by later authors. In the simulated materials by some authors [9, 42, 43, 52], the water bridges between particles are based on the Young–Laplace solution and the sample moisture content is constant, while the toroidal shape water bridge model is also adopted by some other researchers [7] and they obtained similar material behaviours. Furthermore, suction controlled simulations are carried out [47, 48, 58], in which matric suction is constantly maintained through the sample. Recently, Gladky and Schwarze [11] compared the DEM simulation results by using different water bridge model, and it is observed that the macroscopic results are closed to each other. Recently, Melnikov et al. [36] proposed a novel and interesting numerical method with DEM in which they attempted to extend the liquid bridge model to liquid clusters. However, this method can only be applied to relatively static structures (the applied deformation is less than 4%) and the granular packing is mono-sized. Nevertheless, the water bridge model is still a mature way to discuss various micro-features of wet granular materials. So far, the present investigations of wet granular materials by DEM are mainly on a limited number of particle size distributions. Based on laboratory test results, it has already been proven that the grain size distribution has a significant effect on the material hydraulic and strength properties [59, 61]. The material cohesion could be significantly changed if the grain size polydispersity is altered. A systematic study from the grain scale approach is necessary to explain the micro-mechanisms.

Experimental study of the capillary strengthening effect in granular materials can be done through the measurement of the material cohesion or tensile strength. Schubert [49] and Turner et al. [53] measured the tensile strength of wet agglomerates and limestone powder respectively. Furthermore, Pierrat and Caram [41] tested the tensile strength of glass beads, and the experiment results of the tensile strength of wet sands can be seen in [23, 24, 31]. These work quantified the capillary effect in a wide range of water content, and results in the range of low degree of saturation can be referenced for the DEM simulations with a liquid bridge model. On the other hand, the microscopic behaviours of wet granular materials are recently investigated by using X-ray computed tomography. Manahiloh and Muhunthan [34] characterised the orientations of liquid bridges and clusters from the X-ray image as a fabric tensor, and the liquid phase is observed to be an anisotropic

phase. Moscariello et al. [39] investigated the microstructure evolution during the wetting induced collapse of an unsaturated sand. Based on X-ray tomography, Khaddour [22] also points out that the number of liquid bridges or cluster numbers in granular material plays a significant role in the capillary strengthening effect. However, quantitative study of the role of liquid phase microstructure still has limited numbers and a micro-investigation by DEM simulation could be an alternative approach.

The Stress–Force–Fabric (SFF) relationship, firstly proposed by Rothenburg and Bathurst [45], is a theory which explained granular material strength from fabric and force anisotropies characterised by the particle-scale interactions. Its tensorial form is then expressed in [26, 27]. Based on the capillary stress tensor definition [48], which is a homogenisation technique over the liquid bridge effect, a Stress–Force–Fabric (SFF) relationship for wet granular materials has been introduced [57, 62]. This SFF relationship explicitly formulates the macro-stress tensor by the micro-parameters associated with mean particle interactions and anisotropies in the solid phase and water phase, which can be a fundamental theory to analyse the micro-mechanisms of the capillary effect.

The work will carry out a systematic study of capillary strengthening effect on granular materials from macro-behaviours to micro-mechanisms. The main objectives are as follows:

- To validate the capillary bridge model in [57] and [62] by comparing with experiment data and other solutions in the literature.
- To clarify the limit of the pendular regime assumption for different granular assemblies.
- To conduct DEM-based numerical experiments to investigate the capillary strengthening effect.
- To study the effect of particle size, polydispersity and void ratio systematically.
- To discuss the micro-mechanics and effective stress definition in aid of SFF.

2 Numerical simulations

2.1 The capillary bridge model

A complete contact model comprising the capillary effect and the mechanical force induced by the particle contact has been adopted for the DEM simulation. The Hertz–Mindlin model [18, 37] is employed to represent the mechanical force induced by inter-particle deformation and the capillary force is calculated by the suction controlled water bridge model introduced in [57] and [62]. The

toroidal shape approximation is adopted for the liquid bridge shape in which the meridian profile of the water bridge surface is described as a circular arc, which is same to the method I in [12]. In this contact law, the normal contact force F_n is a function of the inter-particle distance D , satisfying the following conditions (Fig. 2a):

- There is no interaction between two particles when $D > D_{\text{rupture}}$ where D_{rupture} is the rupture distance.
- For $0 \leq D \leq D_{\text{rupture}}$ there is only the cohesive capillary force functioning, and the solved capillary bridge force is implemented in the DEM source code by a linear interpolation method.
- When $D < 0$ the normal interactive force is the sum of the attractive capillary force and the repulsive mechanical force. By assuming the inter-particle overlapping is minuscule so that the capillary force is the value as when $D = 0$.

By Young–Laplace equation, the matric suction, which is defined as the difference between air pressure and water pressure ($S = u_a - u_w$), has a relationship with the curvature of the water–air interface as:

$$S = T \left(\frac{1}{r_{\text{ext}}} - \frac{1}{r_{\text{int}}} \right) \quad (1)$$

where the air–water surface tension T is a physical constant ($T = 0.073 \text{ N/m}$ for distilled water at 20°), r_{ext} is the external radius of the toroidal shape meridian profile and r_{int} is the internal radius of the water bridge at the neck as shown in Fig. 2b.

The Young–Laplace equation can also be written in a dimensionless term to represent the scale effect. By normalising the matric suction with the mean particle size \bar{R} and water surface tension T , the dimensionless matric suction S^* is as:

$$S^* = \frac{2\bar{R}S}{T} = \frac{\bar{R}}{r_{\text{ext}}} - \frac{\bar{R}}{r_{\text{int}}} \quad (2)$$

At the same dimensionless suction, the water bridge share the same term of $\left(\frac{\bar{R}}{r_{\text{ext}}} - \frac{\bar{R}}{r_{\text{int}}} \right)$ regardless the particle size. By knowing the normalised inter-particle distance D/\bar{R} , which is related to particle size distribution and void ratio in an assembly, $\frac{\bar{R}}{r_{\text{ext}}}$ and $\frac{\bar{R}}{r_{\text{int}}}$ will be obtained. This means a determined local degree of saturation on one particle pair. Approximately, for granular assemblies, with the same dimensionless suction, the degree of saturation is the same in different samples with parallel particle size distribution and same void ratio. In another word, at the same degree of saturation, the matric suction is inversely proportional to the mean particle size.

For given values of suction, particle size, inter-particle distance and contact angle, the water bridge geometry is

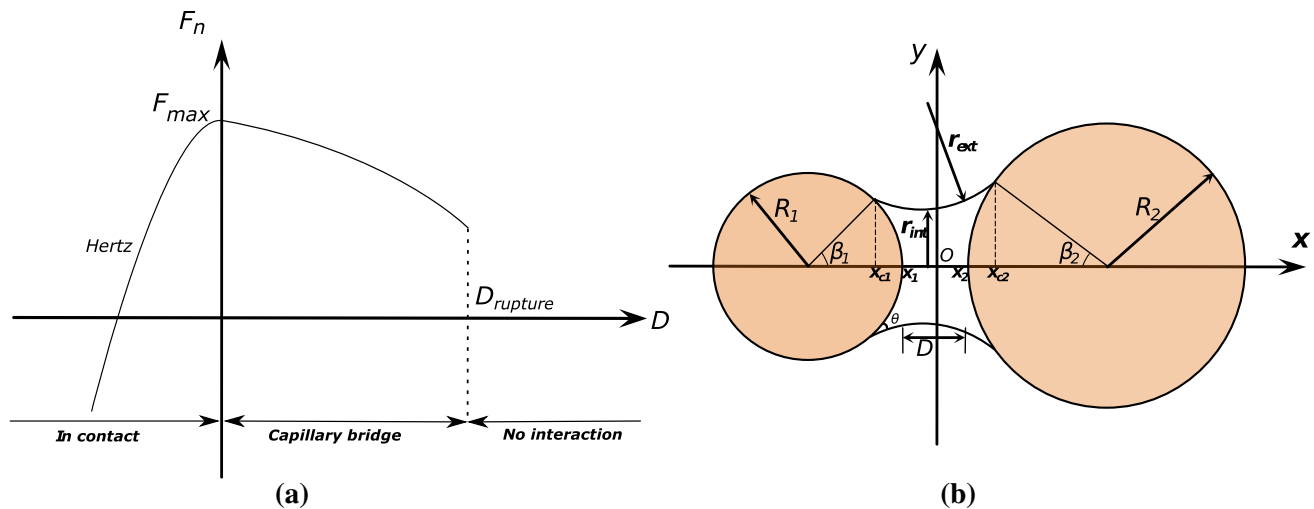


Fig. 2 Water bridge model. **a** Contact law. **b** Water bridge

solved iteratively by the process introduced in [62]. The capillary force can then be obtained by the ‘gorge method’ [20] as the sum of the pressure difference acting on the section of the bridge neck and the surface tension acting on the air–water interface:

$$F_{\text{cap}} = S\pi r_{\text{int}}^2 + T(2\pi r_{\text{int}}) \quad (3)$$

The water volume of the capillary bridge is an integration of the water bridge profile function from x_{c1} to x_{c2} in Fig. 2b, subtracting the volume of the solid between x_{c1} and x_{c2} as:

$$V_{\text{cap}} = \int_{x_{c1}}^{x_{c2}} \pi y^2 dx - \int_{x_{c1}}^{x_{c1}} \pi y_1^2 dx - \int_{x_{c2}}^{x_{c2}} \pi y_2^2 dx \quad (4)$$

where y is the function of the distance between the water surface and the x axis and y_1 and y_2 are functions of the distance between the particle profile and the x axis for particle 1 and particle 2 respectively. In summary, in this water bridge model, suction is a constant input value as suction is assumed to be constant throughout the specimen. The capillary force and liquid bridge volume are determined by the particle pair geometry, inter-particle distance, surface tension and contact angle as $\{F_{\text{cap}}, V_{\text{cap}}\} = f(R_1, R_2, D, S, T, \theta)$.

Besides the toroidal shape approximation, other methods to solve the liquid bridge are mainly on the basis of the numerical solution of the Young–Laplace equation on the mean curvature [28, 47, 48, 51, 52]. In these solutions, the external radius of the liquid bridge is no longer a constant value. By using the ‘gorge method’, these solutions have almost the same value for the capillary force at the same suction (with the same mean curvature at the neck), but the liquid bridge volume solutions differ with each other.

2.2 Comparison with experimental measurements

Gras et al. [13] introduced a suction controlled inter-grain water bridge laboratory test to measure the liquid bridge induced force and the water volume. A water bridge is formed between two metal spheres (5 mm in radius), while the inter-particle distance is adjustable. The air pressure and the pressure in the water bridge are constantly maintained so the suction is controlled at 40, 70 and 140 Pa, respectively. The shape of the water bridge is measured by image analysis, and then the water bridge volume can be calculated by the determined geometry. Due to the water impurity in the experiment apparatus, the water surface tension was measured as 0.051 N/m and the water–solid–air contact angle θ was roughly measured from the image as around 20° . By using the same geometry, surface tension, contact angle and suction parameters above, the experimental tests can be reproduced by the toroidal shape solution we used.

The experiment results by Gras et al. [13] (denoted as ‘exp’) and the toroidal shape numerical solutions (denoted as ‘num’) are compared in Fig. 3. Figure 3a illustrates internal radius r_{int} under different suctions and the capillary forces are compared in Fig. 3b. It can be seen that the rupture distance by the toroidal shape approximation is close to the measured value in the experiment. Slight overestimation on r_{int} and F_{cap} appears at a smaller inter-particle distance by the numerical solution but the discrepancies between the measured and calculated values reduced in higher suction conditions. The higher suction corresponding to a smaller amount of water gives higher accuracy for the numerical solution. Figure 3c compares the experimental and numerical results for water volume between the particles. The numerical solutions based on the

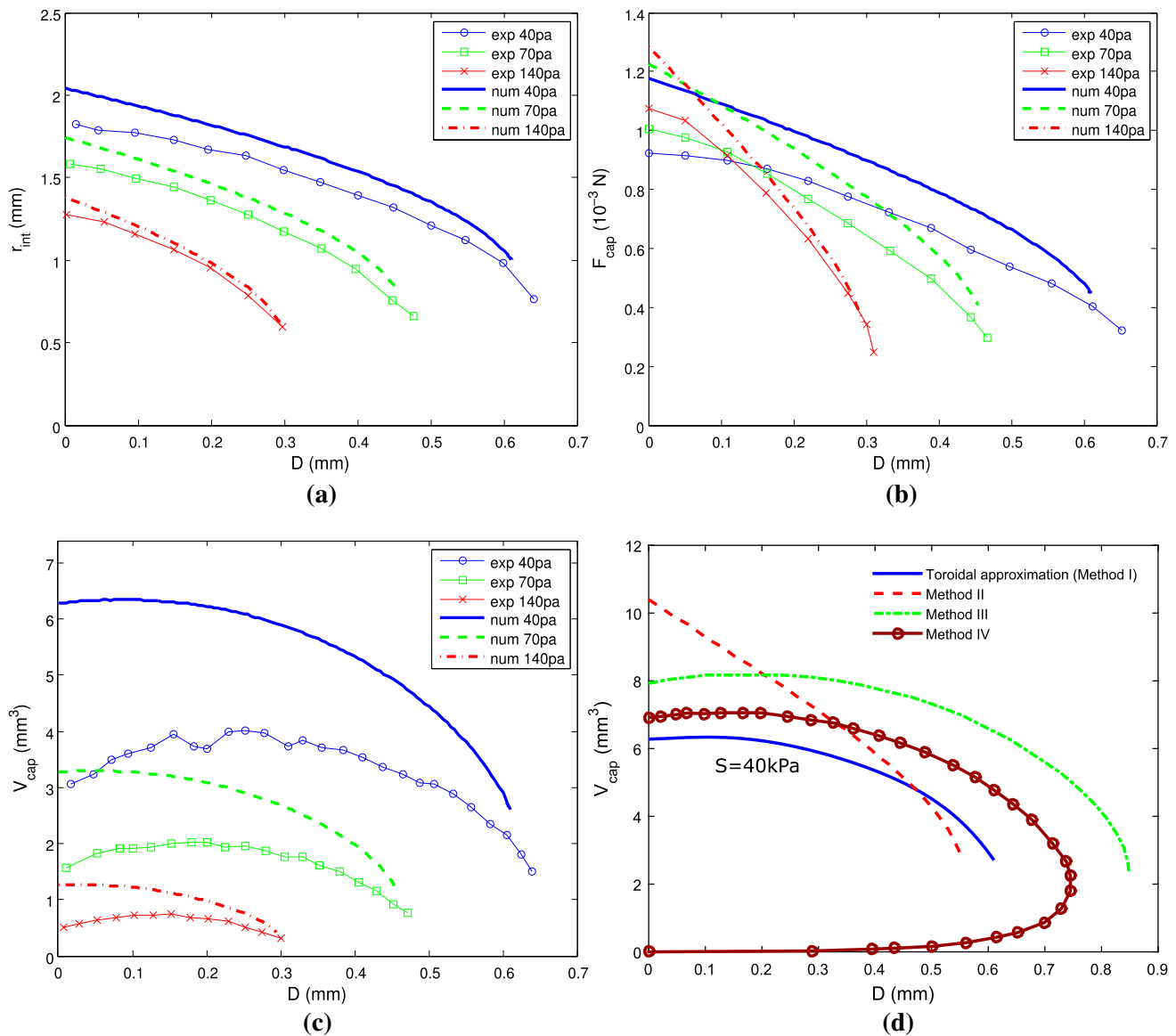


Fig. 3 Comparison between the numerical solution and experimental results of the liquid bridge. **a** Internal radius. **b** Capillary force. **c** Liquid bridge volume. **d** V_{cap} in different methods (after [12])

toroidal approximation overestimate the water bridge volume. A comparison has been made by Gras et al. [12] between different solutions (see the reproduced comparison in Fig. 3d). Method I represents the toroidal shape approximate solution used in this study and methods II, III and IV are numerical solutions [51] based on the differential equations established from Young–Laplace law. Method II is from a fitted equation introduced in [51] and employed in [48] and methods III and IV are based on polynomial (order of 5) and trapezoidal approximations. It can be seen although the toroidal approximation has an overestimation in water bridge volume, it is still the closest solution among the listed methods. For the purpose of representing the capillary effect in DEM simulations, the toroidal shape

numerical solution could be a good choice, with both high practicability and accuracy.

2.3 Granular material properties

The capillary effect from the water bridge between particles is then implemented in the open source DEM code LIGGGHTS [25] to carry out DEM simulations for both dry and unsaturated granular materials. Dry and wet granular packings are simulated in a cubic representative volume element (RVE) surrounded by smooth boundaries with edge length 20 times the mean particle diameter. The total particle number will then be around 10,000, depending on the relative density. The material of the grains in the

simulation is assumed to be quartz. The corresponding parameters are listed in Table 1 in which the inter-particle friction coefficient μ is 0.5, the material density of the grains is 2500 kg/m^3 and Young's modulus and Poisson's ratio of the particles are 70 GPa and 0.2, respectively. The energy dissipation of particle collision is represented by the coefficient of restitution, which is a physical parameter defined as the ratio between the relative velocities between the two particles after and before a collision. In the simulations of wet granular materials, the water phase in the material is assumed to be pure water thus the water–air surface tension is 0.073 N/m (at 20°C).

Table 1 Parameters in the DEM simulation

Water surface tension	0.073 N/m
Water–solid–air contact angle	0
Inter-particle friction coefficient	0.5
Particle density	2500 kg/m^3
Particle Young's modulus	70 GPa
Particle Poisson's ratio	0.25
Particle coefficient of restitution	0.2

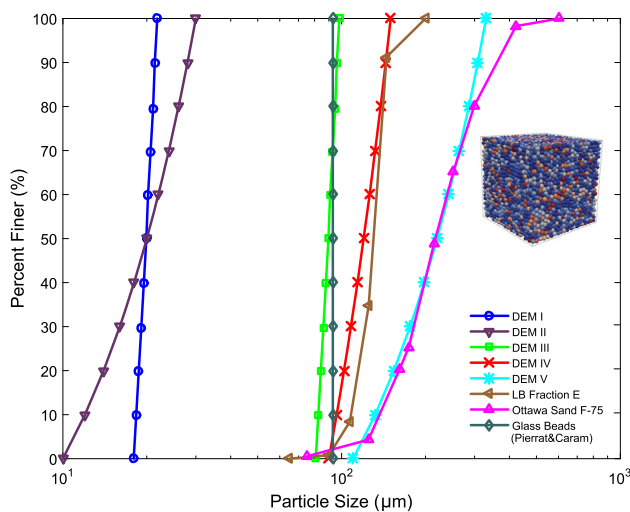


Fig. 4 Particle size distribution

Table 2 Summary of parameters in the tests

Soil type	Particle diameter range (μm)	Void ratio	Matric suction (kPa)						
I	18–22	0.629, 0.688, 0.733	20	50	100	200	300	700	Dry
II	10–30	0.539	20	50	100	200	300	700	Dry
III	81–99	0.629	4.5	11	22	44	67	156	Dry
IV	90–150	0.605	3	8	17	33	50	117	Dry
V	110–330	0.539	2	4.5	9	18	27	64	Dry

There are five kinds of particle size distributions (PSD) studied. The particles are uniformly distributed in percentage by mass from the minimum to the maximum size. Figure 4 plots these PSDs in a passing percentage diagram. Samples I and II are silty sands. Sample III is closed to a glass bead size in an experiment study [41], while the PSDs of IV and V are similar to commercial sands of Leighton Buzzard sand Fraction E and Ottawa sand F-75 respectively. It should be noted that PSDs of samples III and V in DEM are parallel with those of I and II, respectively.

2.4 Sample preparation

The five types of materials (in Fig. 4) are tested in the RVE at four confinements of 10, 20, 100 and 200 kPa, respectively, and both the dry and wet conditions at different matric suction values are simulated. The parameters are summarised in Table 2. The dry specimens are firstly prepared with the specific particle size distributions by using the radius expansion method. Firstly, the particles are inserted into the cell with a reduced particle size from the desired size without contacts. Then, the radii of the particles are expanded to the targeted PSD in several steps. The particle may collide with each other during the expansion and a number of time steps will be run after each expansion to eliminate the motion until the sample reaches to a rather static condition. Inter-particle friction angle is set to be 0 during the expansion to obtain a dense material. After the radius expansion, the inter-particle friction coefficient in different materials is reset to 0.5. For sample type I, two more void ratios (0.688 and 0.733) are generated to investigate the void ratio effect. The inter-particle friction coefficient is set as 0.1 and 0.9, respectively, during the radius expansion process.

Then, the specimens with different void ratios are isotropically compressed to 10, 20, 50 and 100 kPa gradually. Servo-controls are employed for the boundary movement by adjusting the boundary velocity to reach the equilibrium state of the desired stress. The wet specimens are prepared from the dry specimens at each stress level. Without moving the boundary, after applying the capillary model with a specific matric suction value, the cohesive effect bonds the particles together and the stress measured

from the boundary is slightly reduced. Then, a further consolidation will be applied to the wet sample after it reached the equilibrium state of the targeted stress. It has been observed that the void ratio change during this process is negligible.

2.5 Triaxial shear

Then, the triaxial tests on the prepared specimens are following the conventional triaxial loading path in which the lateral pressure (σ_2 and σ_3) is constantly maintained at the corresponding stress level, while the axial strain (ε_1) is increased. The strain increment at each time step is controlled to be small enough to satisfy the ‘quasi-static’ condition. The average unbalance force ratio, which is the ratio between the average unbalance force per particle and the average inter-particle force, is maintained less than 0.01 during the deformation.

Figure 5 plots a set of example results of the dense specimen of sample I with void ratio of $e = 0.629$ at 10 kPa confining stress. The evolution of deviatoric stress $q = \sigma_1 - \sigma_3$ and volumetric strain ε_v of the unsaturated granular materials in the triaxial shearing is plotted. The stress–strain behaviour of the dry specimen with the same void ratio is also presented as a reference.

The capillary effect in the granular soil altered the mechanical behaviour significantly. With the decrease in the matric suction from 5000 to 20 kPa (an increase in water saturation from 0.0012 to 14%), the shear strength of the unsaturated soil raises accordingly from that of the dry soil. The capillary effect also increased the volumetric strain, so that, with the reduction in the suction value, the dilation angle is enlarged. The same triaxial test is implemented on different materials at different stress levels and the mechanical response will be discussed in Sects. 4.

3 Study of hydraulic properties

3.1 Range of the pendular regime

The water retention curves can be obtained by summing up the volume of water bridges and calculating the degree of saturation at different suction values. Due to the limitation of the water bridge model, the range of the pendular state should be clarified. A criterion to check the maximum pendular regime water content based on the half-filling angle is adopted. For two water bridges on a particle (see Fig. 6a) *a* and *b*, the half-filling angles at a particular suction for the two water bridges are β_a and β_b , respectively, and the angle between the two water bridges are α_{ab} . For any two water bridges on the same particle, if $\alpha_{ab} < \beta_a + \beta_b$ that means the two water bridges begin to

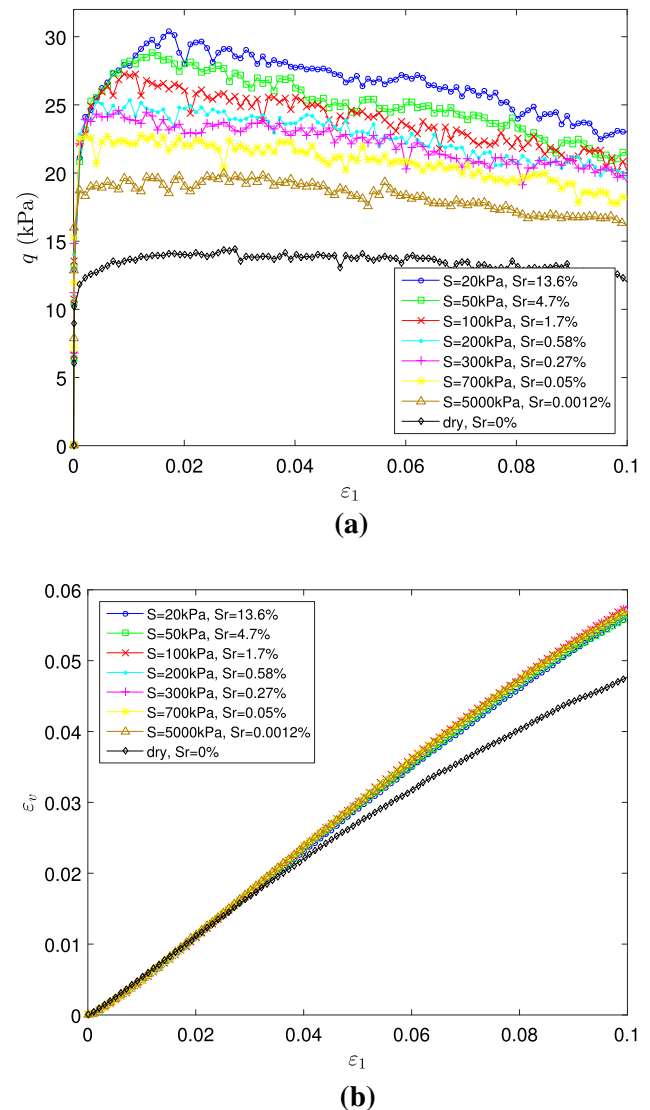


Fig. 5 Typical stress–strain behaviours (sample I with $e = 0.629$ and $\sigma_2 = \sigma_3 = 10\text{ kPa}$). **a** Deviatoric stress. **b** Volumetric Strain

coalesce with each other and the water phase in the specimen reached the funicular state.

Figure 6b shows the relationship between the maximum pendular state degree of saturation and void ratio for different samples. The water–solid–air contact angle is 0. It can be observed that with the increase in the polydispersity in the particle size, the range of the pendular domain will be smaller and with the increase in void ratio the range of the pendular domain is reduced. Another factor may change the pendular regime range is the water–solid–air contact angle. Figure 6c depicts how the range of the pendular regime changes with contact angle. With the increase in contact angle from 0 to 30, the maximum degree of saturation within the pendular regime is increased accordingly. This means for granular materials composed of hydrophilic materials the range of the

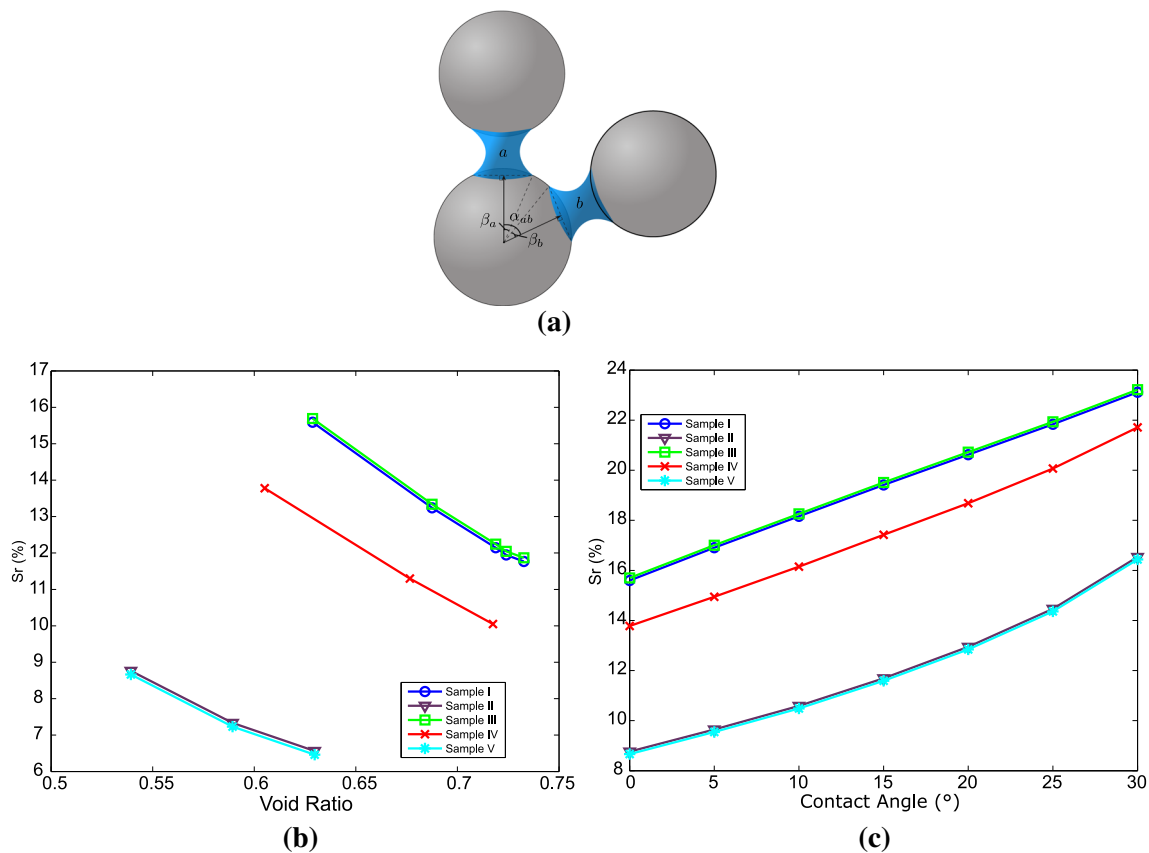


Fig. 6 Maximum degree of saturation within pendular regime. **a** Half-filling angle and water bridge coalescence. **b** Maximum degree of saturation and void ratio. **c** Maximum degree of saturation and contact angle

pendular domain is less than that of a relatively hydrophobic material. It also means that during a drying path, the range of the pendular regime could be smaller than that of granular material in wetting. In the rest of this article, the contact angle is set to be 0 as a conservative choice.

3.2 Water retention curves

The water retention curves of the isotropic samples at 10kPa total stress are plotted in Fig. 7a. It can be seen that for samples I and II, relative density has a great impact on the water retention curve that with a denser sample, the water content is higher at the same matric suction. For sample III, IV and V, as they have much larger grain size, the water retention curves are shifted to the left which means to reach the same water content the matric suction value is inversely proportional to the mean particle size.

The water retention curves are converted into normalised forms (normalised matric suction as $\frac{2RS}{T}$) in Fig. 7b to avoid scale effects. It can be seen from samples II, IV and V that with larger polydispersity it has slight higher water content at the same normalised suction. Yang

et al. [63] measured the drying and wetting path water retention curves for a gravelly sand with 4.7 mm mean diameter and a fine sand with 0.3 mm mean diameter. The experiment results are also compared with the DEM simulation results in the normalised form. It can be found that the normalised curves for sand and gravel are close to each other after adopting the normalised suction definition. It is also observed that the granular assemblies consisting of capillary bridged spheres have a soil water retention property relatively close to those of fine sand and gravel on wetting. This implies that during the drying process the water phase of an unsaturated soil is distributed more continuously in which water clusters may exist. This causes a higher degree of saturation for soils in drying path. Due to the limitation of the numerical model (water bridges are isolated and suction is uniform), the hysteresis effect can only be considered by contact angle change. For wet granular materials with larger contact angles, the degree of saturation is even lower at the same suction [6, 12] and the contact angle effect is much less sensitive than the drying-wetting hysteresis in laboratory experiments. Thus, the capillary bridge models without considering water clusters may only be suitable for the wetting path.

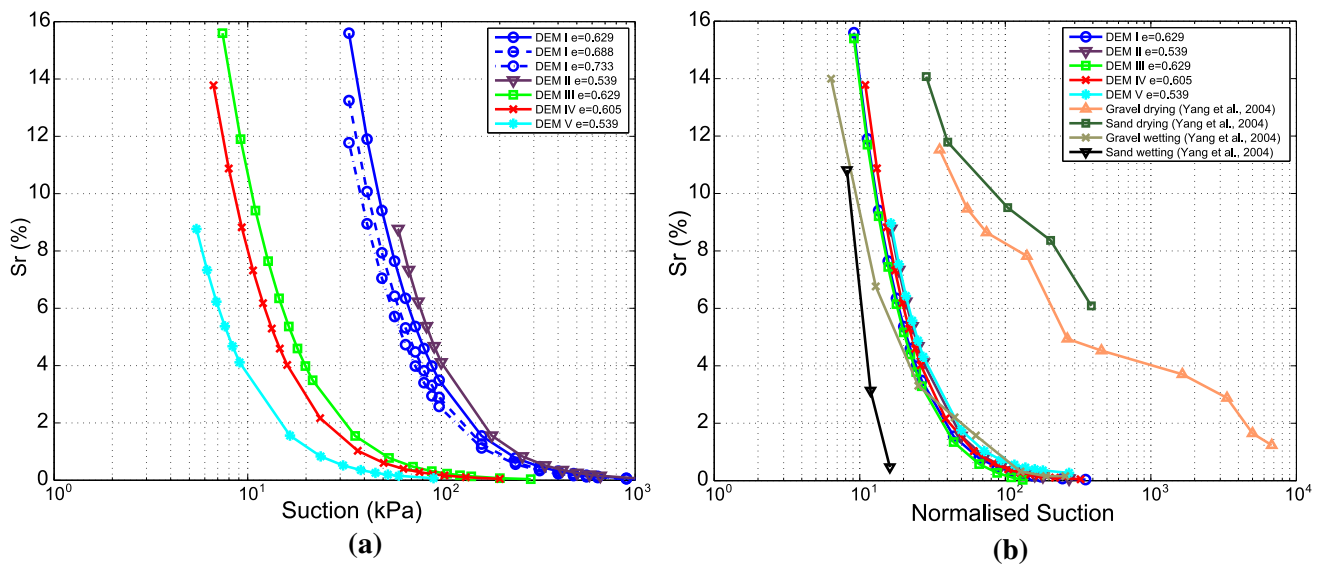


Fig. 7 Water retention properties. **a** Water retention curves. **b** Comparison with experiments in normalised form

3.3 Water bridge distributions

The liquid bridge distributions for the isotropic specimens can be investigated by characterising water bridge numbers on each particle. The probability density distributions of the water bridge number on each particle are plotted in Fig. 8. In Fig. 8a, b, c, the water bridge distributions for samples III, IV and V are illustrated with the increase in water content (S^* is normalised suction) and the dry state distributions of solid contact numbers on each particle are plotted as references. It can be seen that with the decrease in matric suction (increase in water content) the probability density distributions of water bridge number per particle are shifted to the right side. This means a higher average water bridge number in the assembly and the possible maximum water bridge number on a particle is also raised correspondingly. At the dry state, there are small particles do not contact with any other particles as the gravity effect is not included in this study. With the increase in size polydispersity, the number of particles without a physical contact increased from 5% in sample III to 30% in sample V. This means the smaller particles are filled in the space between the large grains without support the granular structure and the stress transmission is mainly through the large particles as investigated by Voivret et al. [54, 55].

Figure 8d illustrates the probability density distributions of water bridge numbers on particles at the maximum water content within the pendular domain. For samples I and III, with a relatively narrow particle size distribution, the water bridge number distribution is like a normal distribution and with the increase in the void ratio the mean water bridge number per particle reduced accordingly. The possible maximum water bridge number is not affected by the void ratio and

stays at 12. From samples I, III and IV to samples II and V, the particle size polydispersity is increased and the particle size span is getting wider. It can be seen that with the increase in particle size span, the water bridge number distribution changed from a normal distribution to a Gamma distribution, in which the distribution is no longer symmetric with the peak value reduced from 8 to 5 and the maximum water bridge number on a particle increased from 12 to 19. It is easy to understand that for a large grain, there could be more water bridges connecting it with surrounded smaller grains.

4 Material strength of wet granular materials

4.1 Contact and capillary stresses

In the particle scale, the inter-particle interaction in a wet granular material is raised from the mechanical contact force and the capillary force as $F = F_{\text{cont}} + F_{\text{cap}}$. The mechanical contact force is originated from the grain deformation on the contact, and it is pushing the neighbouring particle away, so that it is a repulsive force. On the other hand, the capillary force is attractive force. Therefore, F_{cont} and F_{cap} have opposite signs. Scholtès et al. [48] interpreted the stress tensor as the sum of the contact stress tensor and capillary stress tensor by the homogenisation techniques. This definition is followed by Wang et al. [62], and it can be expressed as:

$$\sigma_{ij} = \sigma_{ij}^{\text{cont}} + \sigma_{ij}^{\text{cap}} = \frac{1}{V} \sum_{c \in V} v_{\text{cont}_i}^c F_{\text{cont}_j}^c + \frac{1}{V} \sum_{w \in V} v_{\text{cap}_i}^w F_{\text{cap}_j}^w \quad (9)$$

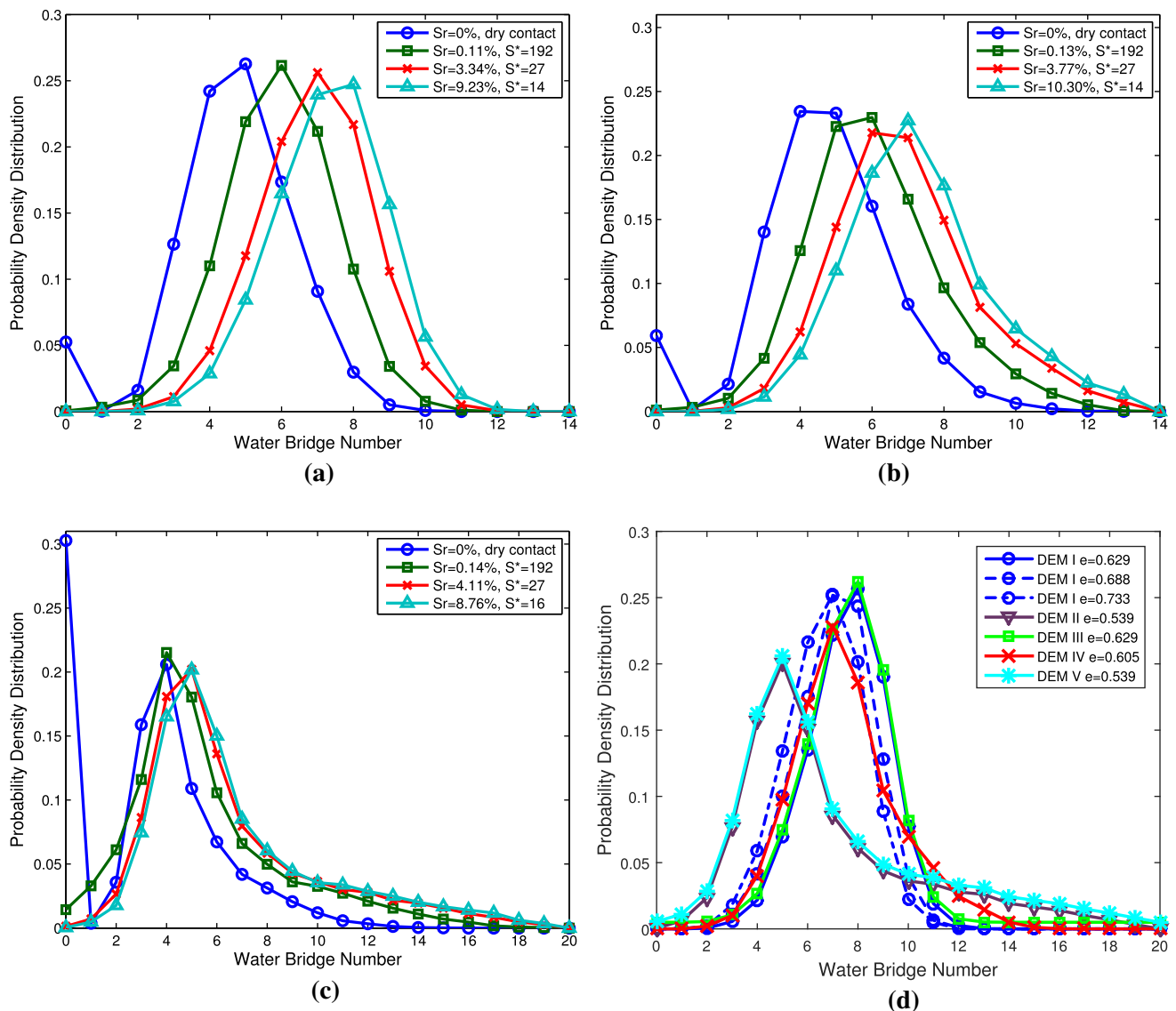


Fig. 8 Water bridge distributions. **a** Soil III. **b** Soil IV. **c** Soil V. **d** At the pendular limit

where c and w are denoting the c -th solid contact and w -th water-particle interaction respectively, V is the total volume, v_{cont} and v_{cap} are vectors pointing from the centre of a grain to the contact or water bridge centre. The positive direction of forces is defined as the acting direction to the particle; thus, the repulsive contact force F_{cont} is positive and the capillary force F_{cap} is negative to the defined direction. The capillary stress tensor represents the stress from matric suction and the contact stress, $\sigma_{ij}^{\text{cont}} = \sigma_{ij} - \sigma_{ij}^{\text{cap}}$, has been regarded as the ‘effective stress’ [47]. Although it has some limitations to determine the volumetric strain [3, 4], it has already provided a good description in the failure mode [47, 56], which can be a useful quantification of the material strength.

By considering the capillary bridge effect, water content change in a granular material alters the capillary stress and the contact stress. Figure 9 illustrates the relationship between the degree of saturation and the mean capillary stress as well as the mean contact stress for the simulated isotropic specimens under 10 kPa mean stress. It can be seen that with a minuscule amount of water added into the dry materials, the absolute value of capillary stress and the effective stress increased significantly. But further increase in moisture content doesn’t change the capillary and contact stresses. Comparing with Figure 4, it can also be seen that for the same degree of saturation, samples with finer particle size have higher matric suction/capillary stress thus stronger contact stress. For same mean particle size, increase the particle size polydispersity (see samples I and II) also raises the capillary effect.

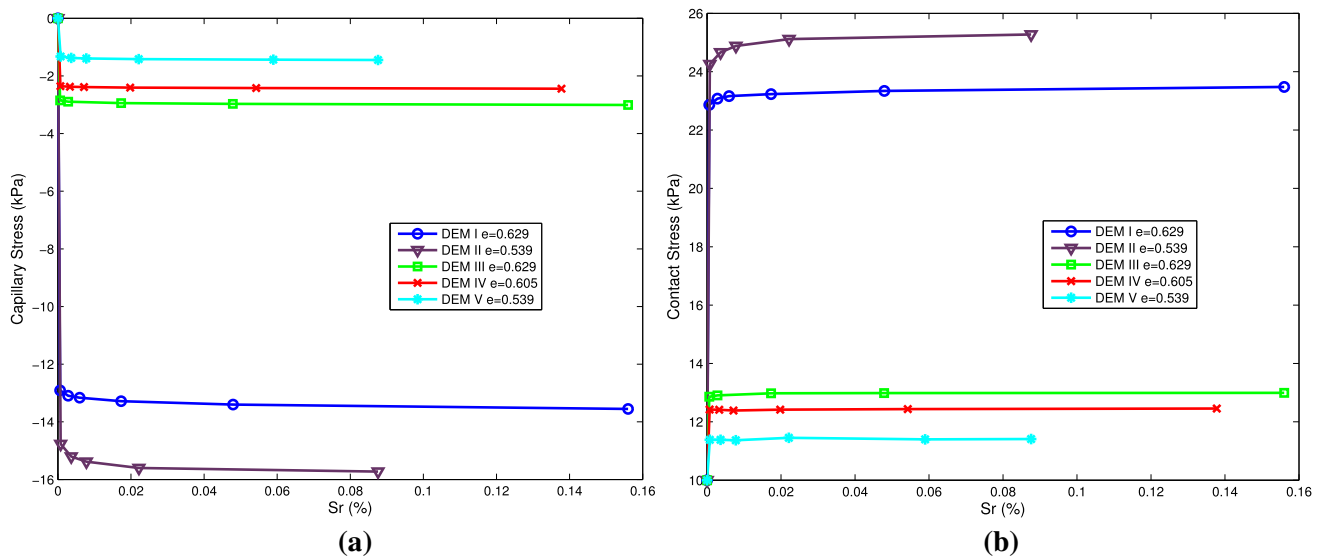


Fig. 9 Capillary stress and contact stress. **a** Capillary stress. **b** Contact stress

4.2 Mohr–Coulomb type failure

By calculating $(\sigma_1 + \sigma_3)/2$ and $(\sigma_1 - \sigma_3)/2$ at peak strength for different confining pressures ($\sigma_3=10, 20, 50$ and 100 kPa respectively). The relationship between shear strength and stress level can be approximately illustrated. Typical results for dry and wet granular materials are represented in Fig. 10 and Fig. 11 in which the results of sample I and II are depicted in Fig. 10 and the results of materials with a larger particle size (sample III, IV and V) are shown in Fig. 11. It can be seen that the results of the unsaturated specimens are almost parallel to that of the dry material, which is linearly increased with the mean stress. This means that the failure mode of wet granular materials can also be described by the Mohr–Coulomb theory. In Fig. 11, as the particle size is larger, the capillary effect is smaller. We will discuss this aspect in the later subsections.

The slopes of the illustrated lines in Fig. 10 and Fig. 11 (usually noted as K_f lines) are correlated to friction angles. Figure 12 demonstrates the relationship between K_f line and Mohr–Coulomb failure envelop. Geometrically, the slope K_f has a relationship with the friction angle ϕ as:

$$K_f = \frac{\sigma_1 - \sigma_3}{\sigma_1 + \sigma_3} = \sin\phi \quad (6)$$

By the above equation, the friction angles for the different materials can be obtained and they are summarised in Table 3. It can be seen that the capillary effect at different degree of saturations does not obviously change the soil friction angle. But the void ratio or sample relative density alters the material peak friction angle significantly. For sample I, the increase in void ratio reduced the friction angle. For sample II, it has a wider particle size distribution

and higher relative density and the friction angle for sample II is larger than that of sample I. For sample III and sample V, they have similar void ratios and parallel particle size distribution to those of sample I ($e = 0.629$) and sample II ($e = 0.539$), respectively, the friction angles for these two samples are also close to those of sample I ($e = 0.629$) and sample II ($e = 0.539$).

4.3 Capillary cohesion and Bishop's coefficient χ

The effective stress of unsaturated soils, firstly proposed by Bishop[2], is formulated as the following form:

$$\sigma'_{ij} = \sigma_{ij} - u_a \delta_{ij} + \chi(u_a - u_w) \delta_{ij} \quad (7)$$

where σ'_{ij} represents the effective stress, σ_{ij} is the total stress, δ_{ij} is the Kronecker delta and χ is the Bishop's coefficient. χ is a value between 0 and 1 depending on soil type and degree of saturation. Based on Bishop's effective stress definition and Mohr–Coulomb theory, by assuming that the friction angle is not changed in unsaturated conditions, shear strength of unsaturated granular materials can be expressed as:

$$\tau = (\sigma_n - u_a) \tan\phi + \chi(u_a - u_w) \tan\phi + c' \quad (8)$$

where σ_n is the total normal stress on the failure plane, ϕ is the friction angle and c' is the effective cohesion for the dry or fully saturated condition. Therefore, the total cohesion can be formulated as:

$$c = \chi(u_a - u_w) \tan\phi + c' \quad (9)$$

From the simulation results, cohesion for materials at the dry state is observed to be negligible. Therefore, in this

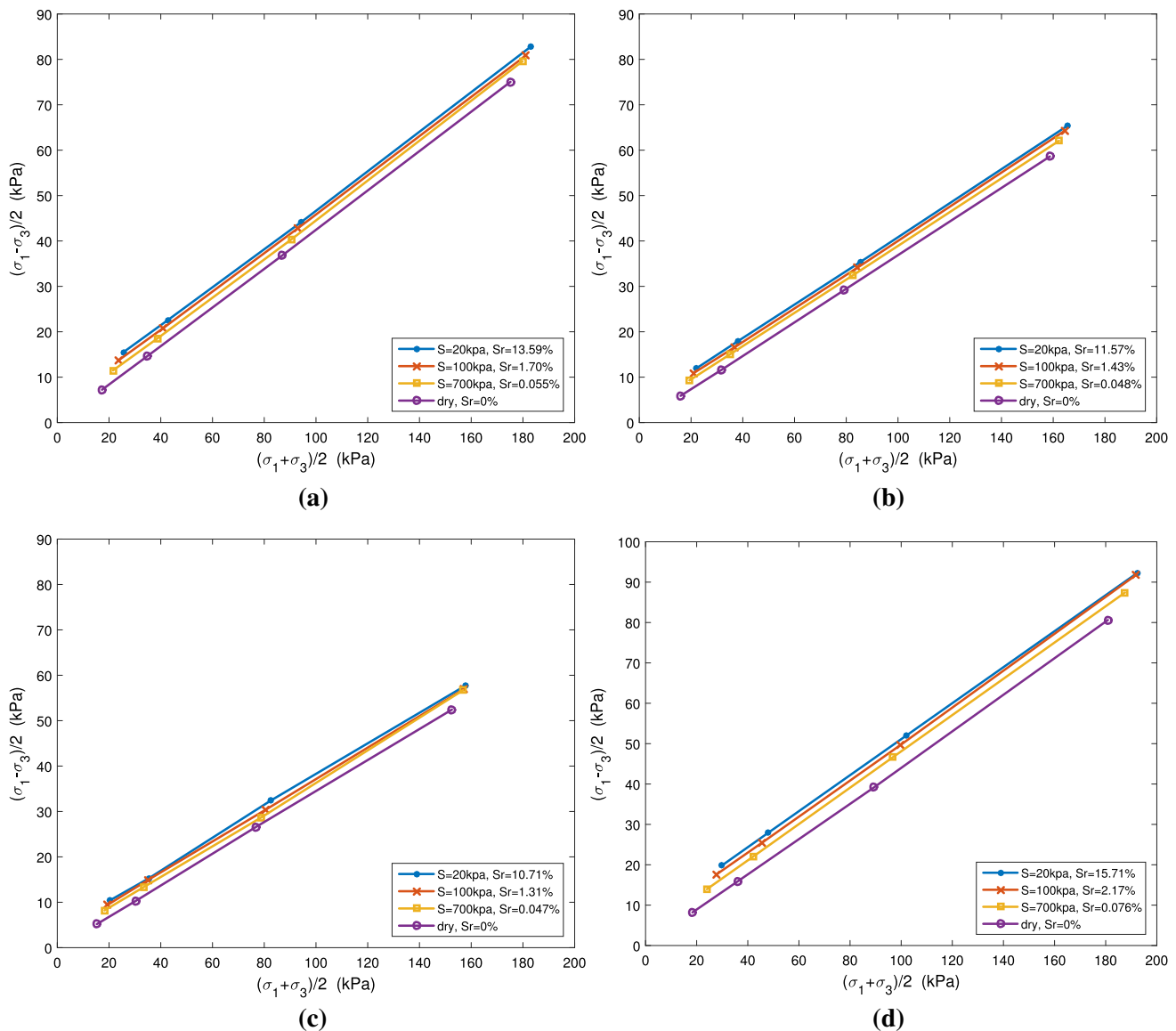


Fig. 10 Relationship between shear strength and stress level for sample I and II. **a** Sample I, $e = 0.629$. **b** Sample I, $e = 0.688$. **c** Sample I, $e = 0.688$. **d** Sample II, $e = 0.733$

study, we approximate that $c' \approx 0$ and the total cohesion c is termed as the capillary cohesion.

By extending the K_f line, the intersection value a in Fig. 12 can be obtained. By considering the relationship between K_f and ϕ , the total cohesion (capillary cohesion) can be calculated from a as:

$$c = \frac{a}{\cos \phi} \quad (10)$$

The capillary cohesions of the simulated materials are presented in Fig. 13. For all granular materials, $c \approx 0$ when $S_r = 0$. However, by adding a minuscule amount of water, the cohesion increases significantly and then the cohesion reaches a plateau that further water content raise only slightly increases the material cohesion. It can also be

observed from the results that, for a same material (for example the sample I), a lower void ratio results in a higher cohesion at the same degree of saturation. For materials with the same mean particle size (sample I and II), increase the particle size polydispersity can reduce the void ratio which also significantly raises the capillary cohesion. Whereas the rest samples (III, IV and V) have relatively larger particle sizes, the capillary cohesion becomes weaker. This indicates the capillary induced cohesion is inversely proportional to the mean particle size.

Particle size distributions of samples III and V are closed to those of a kind of glass beads [41] and Ottawa sand [24]. In the work of [41] and [24], uniaxial tensile test is implemented for which the Mohr circle can be

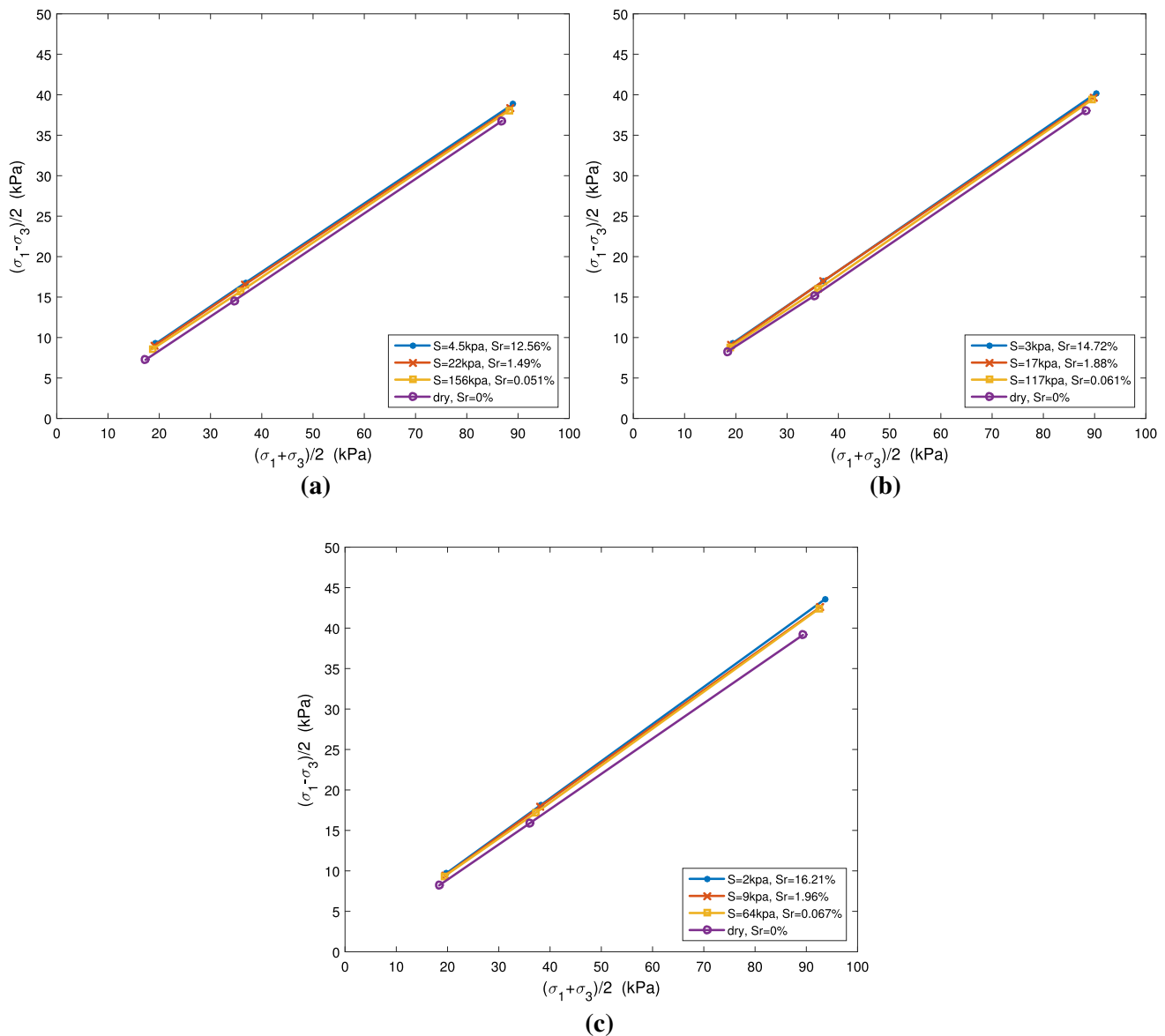


Fig. 11 Relationship between shear strength and stress level for sample III, IV and V. **a** Sample III, $e = 0.629$. **b** Sample IV, $e = 0.605$. **c** Sample V, $e = 0.539$

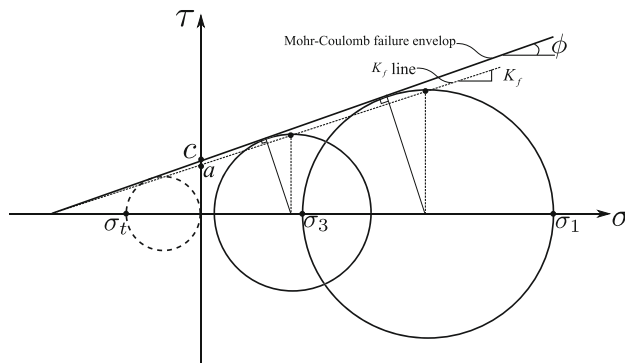


Fig. 12 Conceptual sketch of Mohr-Coulomb failure envelop, K_f line, tensile strength and cohesion

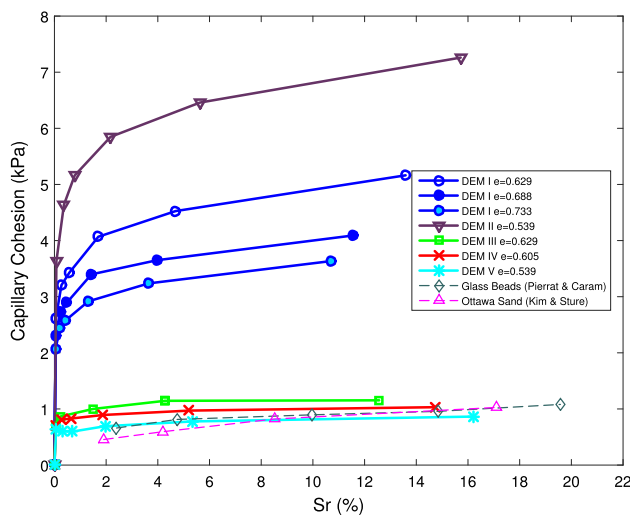
represented by the dash circle in Fig. 12 that the maximum principle stress is zero and the minimum principle stress is the tensile stress. By assuming the Mohr-Coulomb failure envelope is also valid in stress extension domain, the capillary cohesion can be calculated from the tensile strength by the following equation:

$$c = -\frac{\sigma_t}{2 \tan(\frac{\pi}{4} - \frac{\phi}{2})} \quad (11)$$

The capillary cohesions adopted from experiments within the pendular regime are also plotted in Fig. 13 for comparison. It can be seen that the experimental results have the same order of values around 1 kPa with those of samples III, IV and V in simulations. The trend

Table 3 Friction angles of dry and wet granular materials

	$S_r = 0\%$	$S_r = 0.04\text{--}0.08\%$	$S_r = 1.31\text{--}2.17\%$	$S_r = 10.71\text{--}16.21\%$	Average
I ($e = 0.629$)	24.8°	25.1°	24.9°	25.4°	25.1°
I ($e = 0.688$)	21.6°	21.6°	21.6°	21.8°	21.6°
I ($e = 0.732$)	20.1°	20.2°	20.2°	19.9°	20.1°
II ($e = 0.539$)	26.2°	26.6°	26.6°	26.5°	26.5°
III ($e = 0.629$)	24.8°	25.2°	25.2°	25.3°	25.1°
IV ($e = 0.605$)	25.2°	25.6°	25.9°	25.8°	25.6°
V ($e = 0.539$)	26.2°	26.7°	27.3°	27.3°	26.9°

**Fig. 13** Capillary cohesion in simulations and experiments

qualitatively agrees with the simulation results that glass beads specimen (sample III) has higher cohesion than that of Ottawa sand (sample V). The overestimation in DEM simulations may be induced by the following reasons:

- The Mohr–Coulomb failure criterion simplifies the failure strength and mean stress as a linear relationship. However, as discussed by Lu et al. [32], for small stresses or in the tensile domain, the slope of Mohr–Coulomb envelope may become steeper.
- The impurity of water and the temperature change in laboratory may vary the water surface tension which subsequently changes the strength.
- It has been observed by environmental scanning electron microscope (ESEM) that, in sand, the water menisci between particles may be in not only concave shapes but also convex shapes [30]. The convex shape liquid bridges may offset part of the capillary strengthening effect.
- The hydraulic history of the material may induce uncertainties on the relationship between matric suction

and water saturation, while the DEM result has just one possible water retention curve.

Nevertheless, DEM simulation is still a useful tool to discuss the capillary effect in unsaturated granular materials at least on the qualitative level. Another benefit of the DEM method is its insight into the particle scale and physical mechanisms, which will be discussed in the next section.

By knowing capillary cohesion and the corresponding suction, Bishop's coefficient of χ for the simulated materials can be calculated from Eq. 9 in which c' is taken as 0. Figure 14a presents the χ values of the different materials at various degree of saturations. It can be seen that although the simulated materials have different void ratios, polydispersity and mean particle sizes, the basic trend of χ is mainly determined by the degree of saturation and excluding the two scattered points the main trend can be fitted by a third-order polynomial equation as:

$$\chi = 100S_r^3 - 22S_r^2 + 5.6S_r \quad (12)$$

By substituting Eq. 12 into Eq. 9, capillary cohesion is therefore expressed in the following form:

$$c = (100S_r^3 - 22S_r^2 + 5.6S_r)(u_a - u_w)\tan\phi \quad (13)$$

Capillary cohesions predicted by the above equation are illustrated as lines in Fig. 14b with the test results plotted as scatters. They have a fair match with each other for spherical granular materials with different particle size distributions.

5 Micro-mechanism of the capillary strengthening

5.1 The Stress–Force–Fabric relationship for unsaturated granular materials

The Stress–Force–Fabric (SFF) relationship [45] is a theory which formulates the stress tensor by parameters associated with microstructures, force transmission and fabric

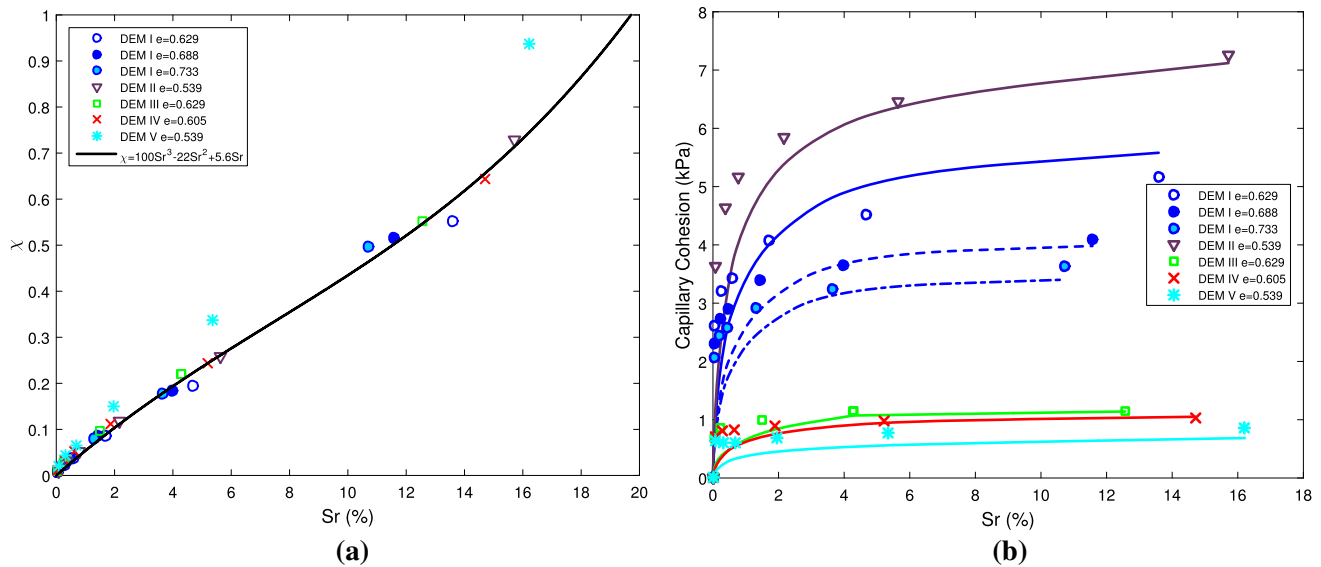


Fig. 14 Bishop's coefficient χ and capillary cohesion. **a** Bishop's coefficient χ . **b** Predicted capillary cohesion

anisotropies. It is recently reintroduced in form of tensor multiplications by considering more complicated loading conditions [26, 27]. For wet granular materials, Scholtès et al. [48] interpreted the stress tensor as the sum of the contact stress tensor and capillary stress tensor. It has been confirmed that the capillary strengthening effect has a coupling effect with the material fabric anisotropy by experiment [14]. By applying the directional statistics theory to examine the information on particle-scale interactions and fabrics obtained from DEM simulations, the Stress–Force–Fabric (SFF) relationship for unsaturated granular materials in pendular states has also been interpreted by characterising the directional distributions associated with the fabrics of solid skeleton and water bridges respectively [57, 62]. In this SFF relationship, the total stress tensor for a representative elementary volume V with N particles is formulated from the microstructures as:

$$\sigma_{ij} = \frac{N\bar{R}}{3V} \left[\omega_s f_{\text{cont}0} \left(\delta_{ji} + G_{ij}^{sf} + \frac{2}{5} D_{ij}^s + \frac{2}{5} D_{im_1}^s G_{jm_1}^{sf} \right) + \omega_w f_{\text{cap}0} \left(\delta_{ji} + \frac{2}{5} D_{ij}^w \right) \right] \quad (14)$$

where \bar{R} is the mean particle radius, ω_s and ω_w are the coordination numbers for solid contacts and water bridges respectively, $f_{\text{cont}0}$ and $f_{\text{cap}0}$ are directional average values for inter-particle contact force and capillary force, and D_{ij}^s , D_{ij}^w , G_{ij}^{sf} are direction tensors representing the anisotropic effects in solid contacts, water bridge directions and contact forces. For a particular material, the mean stress level is mainly determined by coordination numbers of solid contact and water bridge and the mean contact and

capillary force. The stress deviator is mainly represented by the fabric and force anisotropies in the solid and water phases.

For a granular assembly with N_s solid particle contacts, a second rank moment tensor for solid skeleton fabric can be defined by taking an average of the self-tensor product of the unit vector of the inter-particle contact normals as:

$$N_{ij}^s = \frac{1}{N_s} \sum_{c \in V} \mathbf{n}_s \otimes \mathbf{n}_s \quad (15)$$

where \mathbf{n}_s is the unit contact normal vector on c th contact. Similarly, for the water bridge network, a second rank fabric tensor quantifying the unit vectors of the water bridge directions can be defined as an average of the self-tensor product of the unit vector from the water bridge centre to the particle centroid over all water bridges (a total number of N_w and normally $N_w > N_s$):

$$N_{ij}^w = \frac{1}{N_w} \sum_{w \in V} \mathbf{n}_w \otimes \mathbf{n}_w \quad (16)$$

where w is the w th water bridge and \mathbf{n}_w is the unit vector on the water bridge direction. Then, the deviatoric tensors of the solid contacts and water bridges (D_{ij}^s and D_{ij}^w) can be expressed as:

$$D_{ij}^{s/w} = \frac{15}{2} \left(N_{ij}^{s/w} - \frac{1}{3} \delta_{ij} \right) \quad (17)$$

by substituting the corresponding superscripts.

The moment tensor for the directional distribution of contact forces in an assembly (noted as K_{ij}^{sf}) can be defined by an integration of the tensor product of the average contact force along a particular direction noted as $\langle \mathbf{f}_{\text{cont}} \rangle|_{\mathbf{n}_s}$ and the

unit vector of that direction \mathbf{n}_s , and then averaged by the unit sphere surface of Ω :

$$K_{ij}^{sf} = \frac{1}{2\pi} \frac{1}{N_s} \oint_{\Omega} \langle f_{\text{cont}} \rangle |n_s \otimes \mathbf{n}_s d\Omega \quad (18)$$

G_{ij}^{sf} is the deviatoric part of normalised K_{ij}^{sf} as:

$$G_{ij}^{sf} = \frac{3K_{ij}^{sf}}{K_{ii}^{sf}} - \delta_{ij} \quad (19)$$

where K_{ii}^{sf} is the sum of the diagonal line of K_{ij}^{sf} and the directional average of contact force, $f_{\text{cont}0}$, can be approximated as $f_{\text{cont}0} = K_{ii}^{sf}$. The directional average of capillary force, $f_{\text{cap}0}$, is also calculated in a similar way.

The SFF relationship for unsaturated granular materials introduced above is adopted to study unsaturated granular materials. The micro-parameters in this SFF relationship are discussed in the following parts which could explain the micro-origin of the capillary strengthening effect. The materials at the peak strength in the triaxial tests under 10 kPa confining pressure are selected for the investigation.

5.2 Fabric and force anisotropies at peak strength

Firstly, the fabric anisotropies in solid skeleton and water bridges as well as the anisotropic effect in contact forces are investigated. The magnitudes of anisotropies are quantified by the square root of the second tensor invariants for the direction tensors as $\sqrt{3J_2(\mathbf{A})} = \sqrt{[(\mathbf{A}_{11} - \mathbf{A}_{22})^2 + (\mathbf{A}_{22} - \mathbf{A}_{33})^2 + (\mathbf{A}_{33} - \mathbf{A}_{11})^2]/2}$ where \mathbf{A} represents the tensors of D_{ij}^s , D_{ij}^w and G_{ij}^{sf} .

Figure 15 plots the magnitude of fabric anisotropies in the solid contact normals and the water bridge directions at the peak strength in the triaxial tests under 10 kPa confining pressure. In Fig. 15a, the solid phase fabric anisotropies of wet materials at peak strength are even lower than those of dry materials. Beyond 2% degree of saturation, a greater amount of water in the soil only slightly increases the solid phase fabric anisotropy. Moreover, the water bridge network also becomes anisotropic under triaxial loading, but the fabric anisotropies in the water bridge directions are reduced by more water content in the soil specimen. The solid and water phase fabric anisotropies have coupling effect. This means although the capillary effect is also anisotropic, its smaller magnitude offsets the magnitude of the anisotropy in the solid phase.

The contact force anisotropies at the peak strength are depicted in Fig. 16. It can be seen that the anisotropy of solid contact forces is generally increased by more water in the sample. The anisotropy increase in a denser specimen is

more significant than those in a looser material (comparing specimens of sample I). For a material with higher particle size polydispersity, the anisotropic effect of contact forces is stronger at the peak strength (comparing I with II). By looking at the results of samples III, IV and V, it can be seen that with the mean particle size increase generally the contact force anisotropy becomes more significant to the material strength.

5.3 Coordination number at peak strength

Figure 17 illustrates the water content effect on the peak state solid contact coordination number and the water bridge coordination number. It can be seen that with a minuscule amount of water, the capillary effect significantly increased the solid phase coordination number from around 3 to 4 to around 5, while the solid phase coordination number is not obviously changed by further water content increase. The coordination number of the water phase increased accordingly with moisture content and the void ratio has a significant effect on the water phase coordination number, as dense specimens have more water bridges at the same degree of saturation.

Due to the significant influence of the solid coordination number on effective stress, the capillary effect on solid coordination number should be investigated clearly at the particle scale. We analysed the coordination number on each particle statistically. Figure 18 plots the probability density distribution of the possible solid coordination numbers on each particle for the dry and wet samples at the peak state. It can be seen in the dry specimens, without the gravity effect, some particles are not in contact with others. If the granular material is mono-sized material, with a certain confinement, all the particles should be in touch with its neighbouring grains as the particles are regularly arranged. With the increase in grain size polydispersity, the possibility of no contact (0 coordination number) is increased. This is because for a sample with a wider particle size distribution there will be more particles filled in the voids surrounded by larger grains. The finer particles filled in the voids do not support the main structure as forces are mainly transmitted by large grains. In the wet samples, due to the cohesive capillary force, the finer particles in the voids are in touch with their neighbouring particles. The minimum solid coordination number in the assembly is 1 and the maximum coordination number is also increased. In wet samples, the maximum coordination number is also enlarged by a wider particle size range.

In Figure 19, the relationship between the relative particle size and its coordination number is investigated in the dry and wet granular materials at peak state. We use $\frac{R-R_{\min}}{R_{\max}+R_{\min}}$ to represent the relative size of a particle where

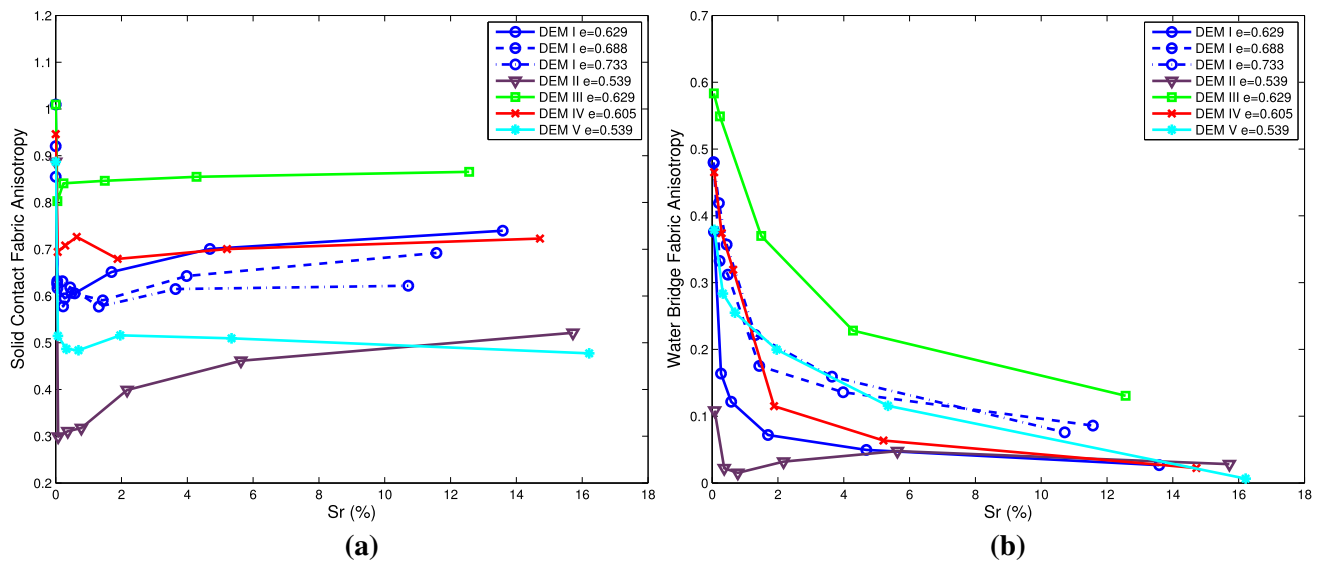


Fig. 15 Fabric anisotropies at peak strength. **a** Solid fabric anisotropy. **b** Water fabric anisotropy

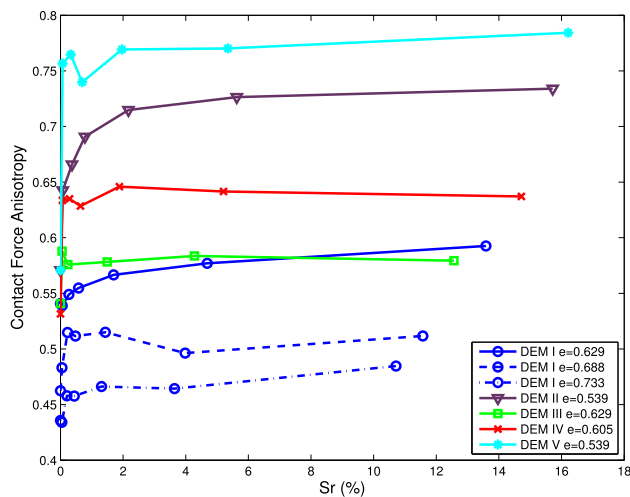


Fig. 16 Solid contact force anisotropy

R_{\max} and R_{\min} are the maximum and minimum particle radius in the specimen. The relative size value is divided into 50 segments, and the average coordination numbers for different relative particle sizes are calculated. In the dry specimens, the coordination number is increased with the relative particle size as a linear relationship. The slope of the relationship between the coordination number and relative particle size is increased by the particle size span. In the wet granular materials, the coordination number is increased on all particles by the cohesive capillary force. The coordination number increase is more significant on larger particles in samples with a wider particle size span. The decrease in mean particle size also consolidated the coordination number increase slightly (comparing sample II with sample V).

We use a parameter of particle size polydispersity κ to characterise the relationship between coordination number and particle size, where $\kappa = \frac{R_{\max} - R_{\min}}{R_{\max} + R_{\min}}$. In dry granular materials, it can be formulated as a linear relationship:

$$\omega_s^{\text{dry}}(R) = 12\kappa \frac{R - R_{\min}}{R_{\max} + R_{\min}} - 6\kappa + 4 \quad (20)$$

where the constant 4 indicates that for a particle with the size around the mean size in the material, its most possible coordination number will be 4, which is the minimum stable coordination number in three-dimensional space. In wet materials, the coordination number function has an additional term added to that of the dry materials. We use a quadratic function to fit the capillary effect on the coordination numbers. It can be expressed as:

$$\omega_s^{\text{wet}}(R) = \omega_s^{\text{dry}}(R) + m\kappa^3 \left(\frac{R - R_{\min}}{R_{\max} + R_{\min}} - 0.2 \right)^2 + 4\kappa^2 + n \quad (21)$$

where m is related to water bridge curvatures and n is inverse proportional to the mean particle size.

5.4 Inter-particle force at peak strength

The mean inter-particle force in different materials under the influence of water are investigated on the parameters of $f_{\text{cont}0}$ and $f_{\text{cap}0}$ which represent the level of mean contact force and mean capillary force respectively. Figure 20 demonstrates the water content effect on $f_{\text{cont}0}$ and $f_{\text{cap}0}$ for the simulated materials at peak state under 10kPa confining stress. Figure 20a shows the change of the $f_{\text{cont}0}$ from that of the dry sample in percentage with the increase in degree of saturation. For finer materials, like I, II and III, adding

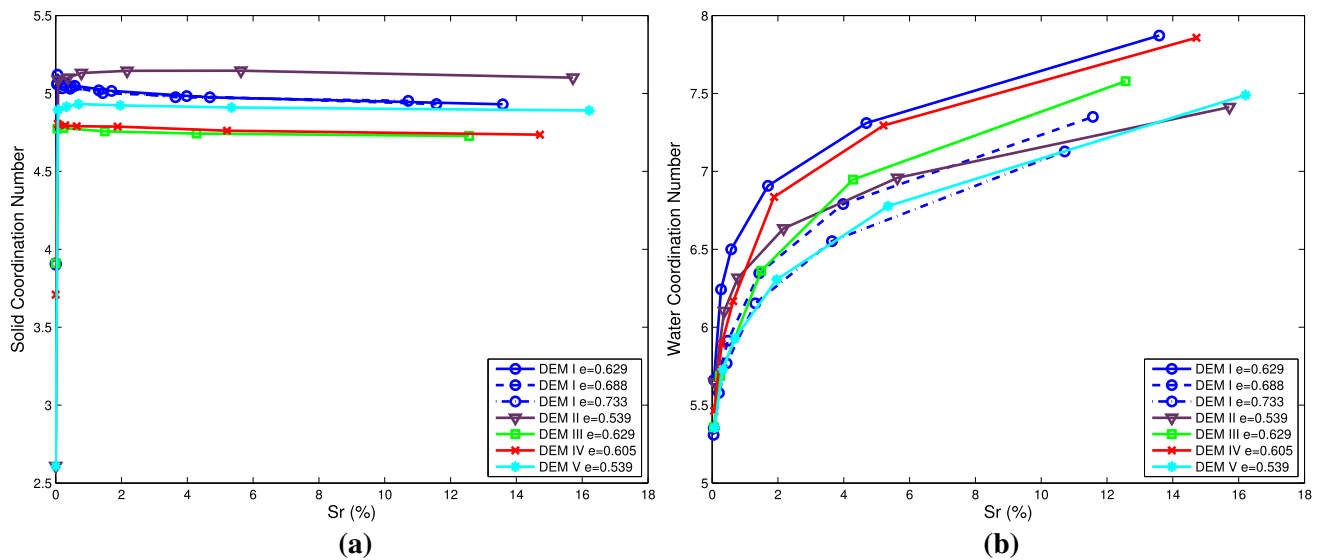


Fig. 17 Coordination numbers at the peak strength. **a** Solid coordination number. **b** Water coordination number

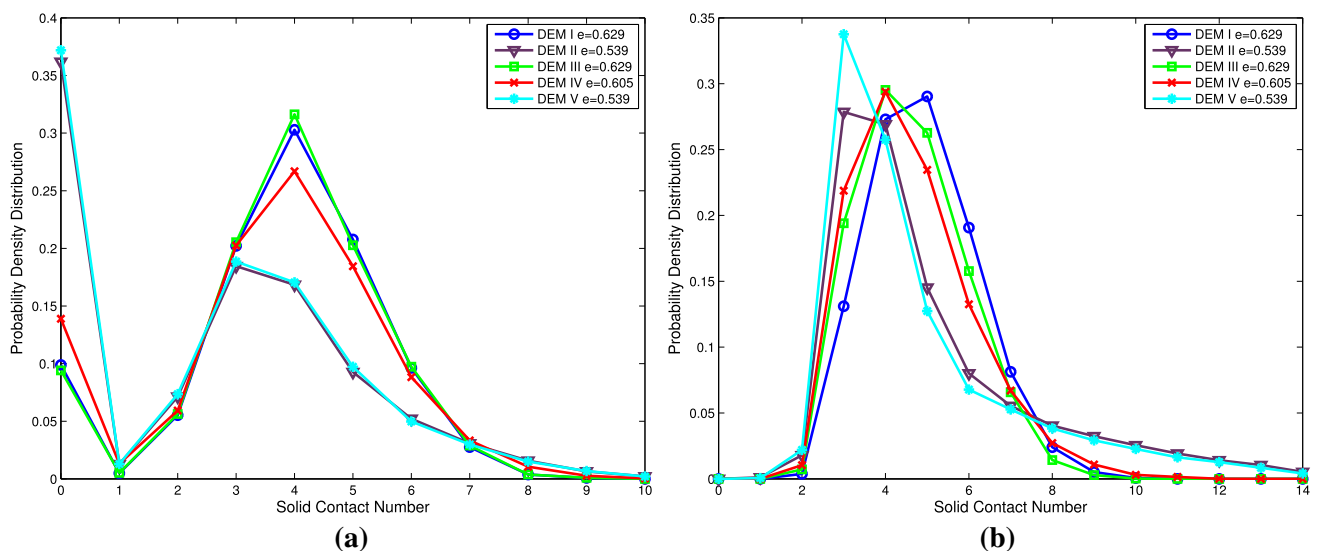


Fig. 18 Probability distribution of solid coordination numbers on each particle. **a** $S_r = 0\%$. **b** $S_r \approx 2\%$

water will increase the mean contact force which is correlated to the capillary strengthening effect. However, for a coarser material, such as sample IV and V, the capillary effect will not obviously increase the mean contact force level. This is because the capillary effect increased the solid coordination number, but the contact force on the new contacts is relatively small.

Figure 20b depicts the absolute values of the ratio between f_{cap0} and f_{cont0} at various degree of saturation. It can be seen that with the increase in water content, the mean capillary force level is a decreasing trend. This is

because most of the particle pairs with a water bridge have relatively small inter-particle distance and the increase in water content (decrease in matric suction) extended the rupture distance but weakened the capillary force when it has small inter-particle distance (see Fig. 3). It can also be observed that for samples with larger mean particle size, the value of $\left| \frac{f_{cap0}}{f_{cont0}} \right|$ is smaller. This means for materials composed of larger grains, the capillary effect on inter-particle force is smaller comparing to the effect on finer soils.

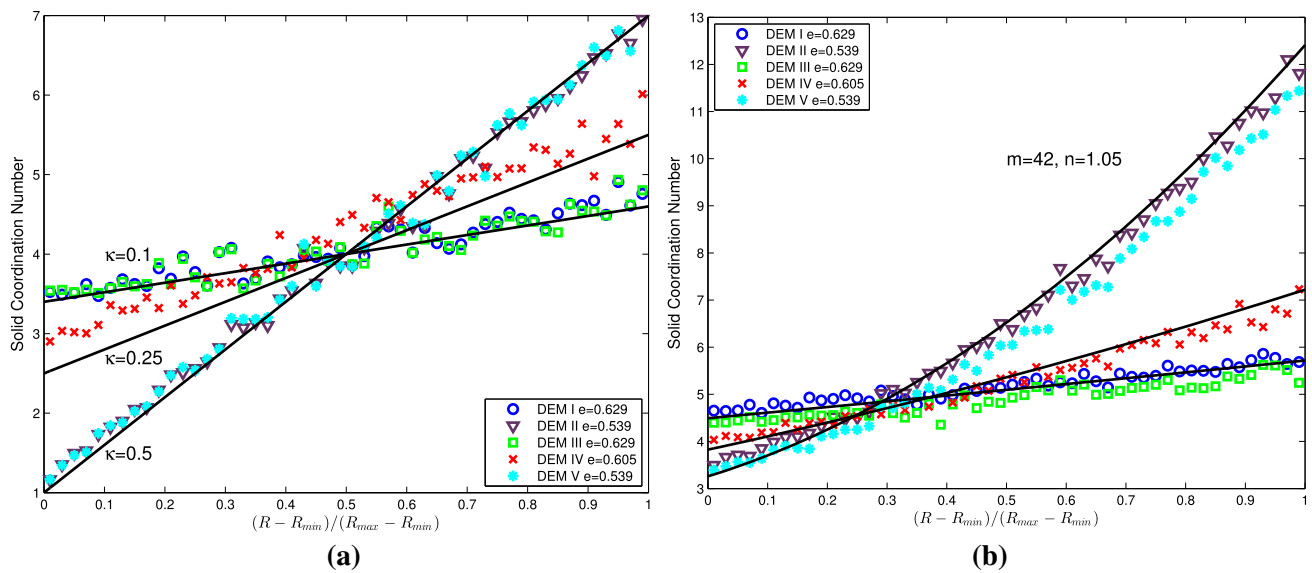


Fig. 19 Average solid coordination number versus normalised particle size. **a** $S_r = 0\%$. **b** $S_r \approx 2\%$

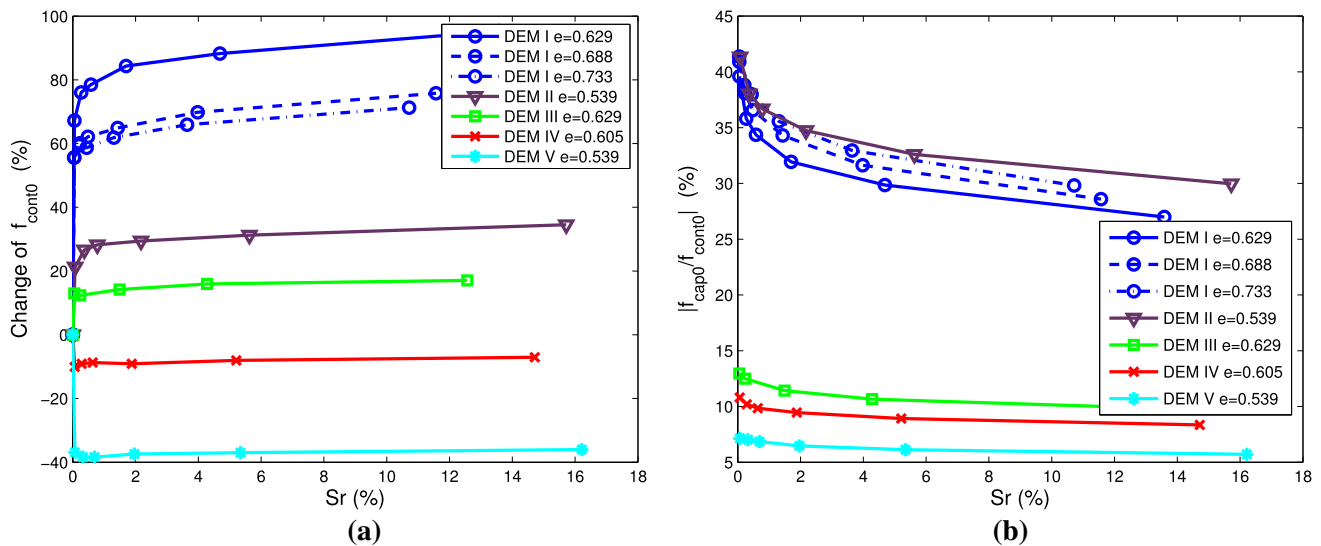


Fig. 20 Inter-particle contact and capillary force. **a** Water effect on $f_{\text{cont}0}$. **b** Water effect on $f_{\text{cap}0}$

6 Summary and conclusions

By introducing capillary bridge effect between particles, wet granular materials are simulated by DEM method in a triaxial loading path to investigate the capillary strengthening effect and its micro-mechanisms. The water bridges are approximated as toroidal shape, and the assumption is proven to be acceptable by comparing with experiments in the literature. Granular materials with different void ratios and particle size distributions are systematically investigated in this study.

The limit of the pendular state is discussed based on the occurrence of water bridge coalescence. Larger void ratio and particle size polydispersity lead the limit of pendular

state to a lower degree of saturation. The contact angle hysteresis also affects the range of the pendular state that higher contact angle means larger pendular state range. By comparing the simulated water retention property with experiment, it supports that the widely used water bridge model is more suitable to simulate a material in the wetting path.

The capillary effect on mechanical behaviours is discussed based on triaxial tests. Water content does not obviously alter the material friction angle which is mainly affected by void ratio and particle size polydispersity. The capillary induced cohesion is increased sharply by a minuscule amount of water, but further increase in moisture content only strengthens the material slightly. A

relationship between the Bishop's coefficient χ is obtained from the simulations on different granular materials. The capillary cohesion is therefore in function of degree of saturation, matric suction and friction angle. At the same degree of saturation, cohesion is inversely proportional to mean particle size and strengthened by higher particle size polydispersity.

The micro-mechanism of capillary strengthening effect is discussed after the SFF relationship. At the peak strength, solid contact fabric, water bridge fabric and contact force distribution are anisotropic due to the loading. Water content increase makes the contact force more anisotropic at peak state. However, more water in a material means less anisotropic effect in water phase fabric. Solid contact number and mean solid contact force are associated with the effective stress. Distributions of solid contact numbers are analysed statistically, and it revealed that the particle size polydispersity effect on the capillary cohesion is mainly through the coordination number distribution. The ratio between the mean capillary force and mean contact force is increased by reducing mean particle size, since water surface tension is a physical constant at different scales, and this is the main reason why the capillary cohesion is more significant in finer materials.

References

- Alonso EE, Pereira JM, Vaunat J, Olivella S (2010) A microstructurally based effective stress for unsaturated soils. *Géotechnique* 60(12):913–925. <https://doi.org/10.1680/geot.8.P.002>
- Bishop AW, Blight GE (1963) Some aspects of effective stress in saturated and partly saturated soils. *Géotechnique* 13(3):177–197. <https://doi.org/10.1680/geot.1963.13.3.177>
- Chalak C, Chareyre B, Nikooee E, Darve F (2016) Partially saturated media: from DEM simulation to thermodynamic interpretation. *Eur J Environ Civ Eng*. <https://doi.org/10.1080/19648189.2016.1164087>
- Chareyre B, Scholtes L, Darve F, Nakagawa M, Luding S (2009) Micro-statics and micro-kinematics of capillary phenomena in dense granular materials. *AIP Conf Proc* 3:927–930. <https://doi.org/10.1063/1.3180083>
- Cundall PA, Strack ODL (1979) A discrete numerical model for granular assemblies. *Géotechnique* 29(1):47–65. <https://doi.org/10.1680/geot.1979.29.1.47>
- Duriez J, Wan R (2016) Contact angle mechanical influence in wet granular soils. *Acta Geotechnica*. <https://doi.org/10.1007/s11440-016-0500-6>
- El Shamy U, Gröger T (2008) Micromechanical aspects of the shear strength of wet granular soils. *Int J Numer Anal Methods Geomech* 32(14):1763–1790. <https://doi.org/10.1002/nag.695>
- Fisher RA (1926) On the capillary forces in an ideal soil; correction of formulae given by W. B. Haines. *J Agric Sci* 16(03):492. <https://doi.org/10.1017/S0021859600007838>
- Gabrieli F, Lambert P, Cola S, Calvetti F (2012) Micromechanical modelling of erosion due to evaporation in a partially wet granular slope. *Int J Numer Anal Methods Geomech* 36(7):918–943. <https://doi.org/10.1002/nag.1038>
- Gili JA, Alonso EE (2002) Microstructural deformation mechanisms of unsaturated granular soils. *Int J Numer Anal Methods Geomech* 26(5):433–468. <https://doi.org/10.1002/nag.206>
- Gladkyy A, Schwarze R (2014) Comparison of different capillary bridge models for application in the discrete element method. *Granul Matter* 16(6):911–920. <https://doi.org/10.1007/s10035-014-0527-z>
- Gras JP, Delenne JY, Soulié F, El Youssofi M (2011) DEM and experimental analysis of the water retention curve in polydisperse granular media. *Powder Technol* 208(2):296–300. <https://doi.org/10.1016/j.powtec.2010.08.019>
- Gras JP, Delenne JY, El Youssofi MS (2013) Study of capillary interaction between two grains: a new experimental device with suction control. *Granul Matter* 15(1):49–56. <https://doi.org/10.1007/s10035-012-0388-2>
- Guo P (2014) Coupled effects of capillary suction and fabric on the strength of moist granular materials. *Acta Mech* 225(8):2261–2275. <https://doi.org/10.1007/s00707-014-1124-2>
- Haines WB (1925) Studies in the physical properties of soils: II. A note on the cohesion developed by capillary forces in an ideal soil. *J Agric Sci* 15:529–535. <https://doi.org/10.1017/S0021859600082460>
- Haines WB (1930) Studies in the physical properties of soil: V. The hysteresis effect in capillary properties, and the modes of moisture distribution associated therewith. *J Agric Sci* 20(01):97–116. <https://doi.org/10.1017/S002185960008864X>
- Harireche O, Faramarzi A, Alani AM (2015) Prediction of inter-particle capillary forces for non-perfectly wettable granular assemblies. *Granul Matter* 17(5):537–543. <https://doi.org/10.1007/s10035-015-0581-1>
- Hertz H (1882) Über die berührung fester elastischer körper. *J für die Reine und Angewandte Mathematik* 92:156–171
- Hornbaker DJ, Albert R, Albert I, Barabási AL, Schiffer P (1997) What keeps sandcastles standing? *Nature* 387(6635):765–765. <https://doi.org/10.1038/42831>
- Hotta K, Takeda K, Iinoya K (1974) The capillary binding force of a liquid bridge. *Powder Technol* 10(4–5):231–242. [https://doi.org/10.1016/0032-5910\(74\)85047-3](https://doi.org/10.1016/0032-5910(74)85047-3)
- Jiang MJ, Leroueil S, Konrad JM (2004) Insight into shear strength functions of unsaturated granulates by DEM analyses. *Comput Geotech* 31(6):473–489. <https://doi.org/10.1016/j.compgeo.2004.07.001>
- Khaddour G (2015) Multi-scale characterisation of the hydro-mechanical behaviour of unsaturated sand: water retention and triaxial response. PhD thesis, Université Grenoble Alpes, France
- Kim TH, Hwang C (2003) Modeling of tensile strength on moist granular earth material at low water content. *Eng Geol* 69(3–4):233–244. [https://doi.org/10.1016/S0013-7952\(02\)00284-3](https://doi.org/10.1016/S0013-7952(02)00284-3)
- Kim TH, Sture S (2008) Capillary-induced tensile strength in unsaturated sands. *Can Geotech J* 45(5):726–737. <https://doi.org/10.1139/T08-017>
- Kloss C, Goniva C, Hager A (2012) Models, algorithms and validation for opensource DEM and CFDDEM. *Prog Comput Fluid Dyn Int J* 12(2):140–152
- Li X, Yu HS (2013) On the stress–force–fabric relationship for granular materials. *Int J Solids Struct* 50(9):1285–1302. <https://doi.org/10.1016/j.ijsolstr.2012.12.023>
- Li X, Yu HS (2014) Fabric, force and strength anisotropies in granular materials: a micromechanical insight. *Acta Mech* 225(8):2345–2362. <https://doi.org/10.1007/s00707-014-1120-6>
- Lian G, Thornton C, Adams MJ (1993) A theoretical study of the liquid bridge forces between two rigid spherical bodies. *J Colloid*

- Interface Sci 161(1):138–147. <https://doi.org/10.1006/jcis.1993.1452>
29. Liu S, Sun D, Wang Y (2003) Numerical study of soil collapse behavior by discrete element modelling. *Comput Geotech* 30(5):399–408. [https://doi.org/10.1016/S0266-352X\(03\)00016-8](https://doi.org/10.1016/S0266-352X(03)00016-8)
 30. Lourenço S, Gallipoli D, Augarde C, Toll D, Fisher P, Congreve A (2012) Formation and evolution of water menisci in unsaturated granular media. *Géotechnique* 62(3):193–199. <https://doi.org/10.1680/geot.11.P.034>
 31. Lu N, Wu B, Tan CP (2007) Tensile strength characteristics of unsaturated sands. *J Geotech Geoenviron Eng* 133(2):144–154. [https://doi.org/10.1061/\(ASCE\)1090-0241\(2007\)133:2\(144\)](https://doi.org/10.1061/(ASCE)1090-0241(2007)133:2(144))
 32. Lu N, Kim TH, Sture S, Likos WJ (2009) Tensile strength of unsaturated sand. *J Eng Mech* 135(12):1410–1419. [https://doi.org/10.1061/\(ASCE\)EM.1943-7889.0000054](https://doi.org/10.1061/(ASCE)EM.1943-7889.0000054)
 33. Lu N, Godt JW, Wu DT (2010) A closed-form equation for effective stress in unsaturated soil. *Water Resources Res* 46(5):W05515. <https://doi.org/10.1029/2009WR008646>
 34. Manahiloh K, Muhunthan B (2012) Characterizing liquid phase fabric of unsaturated specimens from X-ray computed tomography images. In: Mancuso C, Jommi C, D'Onza F (eds) *Unsaturated soils: research and applications*. Springer, Berlin, pp 71–80
 35. Mason G, Clark W (1965) Liquid bridges between spheres. *Chem Eng Sci* 20(10):859–866. [https://doi.org/10.1016/0009-2509\(65\)80082-3](https://doi.org/10.1016/0009-2509(65)80082-3)
 36. Melnikov K, Wittel FK, Herrmann HJ (2016) Micro-mechanical failure analysis of wet granular matter. *Acta Geotech* 11(3):539–548. <https://doi.org/10.1007/s11440-016-0465-5>
 37. Mindlin R (1949) Compliance of elastic bodies in contact. *J Appl Mech* 16:259–268
 38. Mitarai N, Nori F (2006) Wet granular materials. *Adv Phys* 55(1–2):1–45. <https://doi.org/10.1080/00018730600626065>
 39. Moscariello M, Cuomo S, Salager S (2017) Capillary collapse of loose pyroclastic unsaturated sands characterized at grain scale. *Acta Geotech*. <https://doi.org/10.1007/s11440-017-0603-8>
 40. Newitt D, Conway-Jones J (1958) A contribution to the theory and practice of granulation. *Trans Inst Chem Eng* 36:422
 41. Pierrat P, Caram HS (1997) Tensile strength of wet granula materials. *Powder Technol* 91(2):83–93. [https://doi.org/10.1016/S0032-5910\(96\)03179-8](https://doi.org/10.1016/S0032-5910(96)03179-8)
 42. Richefeu V, El Youssoufi M, Radjaï F (2006) Shear strength properties of wet granular materials. *Phys Rev E* 73(5):051304. <https://doi.org/10.1103/PhysRevE.73.051304>
 43. Richefeu V, El Youssoufi MS, Peyroux R, Radjaï F (2008) A model of capillary cohesion for numerical simulations of 3D polydisperse granular media. *Int J Numer Anal Methods Geomech* 32(11):1365–1383. <https://doi.org/10.1002/nag.674>
 44. Rose W (1958) Volumes and surface areas of pendular rings. *J Appl Phys* 29(4):687. <https://doi.org/10.1063/1.1723251>
 45. Rothenburg L, Bathurst RJ (1989) Analytical study of induced anisotropy in idealized granular materials. *Géotechnique* 39(4):601–614. <https://doi.org/10.1680/geot.1989.39.4.601>
 46. Scheel M, Seemann R, Brinkmann M, Di Michiel M, Sheppard A, Breidenbach B, Herminghaus S (2008) Morphological clues to wet granular pile stability. *Nat Mater* 7(3):189–193. <https://doi.org/10.1038/nmat2117>
 47. Scholtès L, Chareyre B, Nicot F, Darve F (2009a) Micromechanics of granular materials with capillary effects. *Int J Eng Sci* 47(1):64–75. <https://doi.org/10.1016/j.ijengsci.2008.07.002>
 48. Scholtès L, Hicher P, Nicot F, Chareyre B, Darve F (2009b) On the capillary stress tensor in wet granular materials. *Int J Numer Anal Methods Geomech* 33(10):1289–1313. <https://doi.org/10.1002/nag.767>
 49. Schubert H (1975) Tensile strength of agglomerates. *Powder Technol* 11(2):107–119. [https://doi.org/10.1016/0032-5910\(75\)80036-2](https://doi.org/10.1016/0032-5910(75)80036-2)
 50. Semperebon C, Scheel M, Herminghaus S, Seemann R, Brinkmann M (2016) Liquid morphologies and capillary forces between three spherical beads. *Phys Rev E* 94(1):012907. <https://doi.org/10.1103/PhysRevE.94.012907>
 51. Soulié F, Cherblanc F, El Youssoufi M, Saix C (2006a) Influence of liquid bridges on the mechanical behaviour of polydisperse granular materials. *Int J Numer Anal Meth Geomech* 30(3):213–228. <https://doi.org/10.1002/nag.476>
 52. Soulié F, El Youssoufi MS, Cherblanc F, Saix C (2006b) Capillary cohesion and mechanical strength of polydisperse granular materials. *The Eur Phys J E Soft Matter* 21(4):349–357. <https://doi.org/10.1140/epje/i2006-10076-2>
 53. Turner G, Balasubramanian M, Otten L (1976) The tensile strength of moist limestone powder. Measurements by different apparatuses. *Powder Technol* 15(1):97–105. [https://doi.org/10.1016/0032-5910\(76\)80034-4](https://doi.org/10.1016/0032-5910(76)80034-4)
 54. Voivret C, Radjaï F, Delenne J, El Youssoufi MS (2007) Space-filling properties of polydisperse granular media. *Phys Rev E* 76(2):021301. <https://doi.org/10.1103/PhysRevE.76.021301>
 55. Voivret C, Radjaï F, Delenne J, El Youssoufi M (2009) Multiscale force networks in highly polydisperse granular media. *Phys Rev Lett* 102(17):178001. <https://doi.org/10.1103/PhysRevLett.102.178001>
 56. Wan R, Duriez J, Darve F (2015) A tensorial description of stresses in triphasic granular materials with interfaces. *Geomech Energy Environ* 4:73–87. <https://doi.org/10.1016/j.gete.2015.11.004>
 57. Wang JP (2015) Discrete element modelling and micromechanics of pendular state unsaturated granular materials. PhD thesis, University of Nottingham, UK
 58. Wang JP, Li X, Yu HS (2015) A micromechanical interpretation of the capillary effect of unsaturated granular material in a pendular state. In: *Proceedings of the 14th international conference of international association for computer methods and recent advances in geomechanics, IACMAG 2014*, Taylor and Francis, Balkema, pp 1563–1568
 59. Wang JP, François B, Lambert P (2017a) Equations for hydraulic conductivity estimation from particle size distribution: a dimensional analysis. *Water Resour Res* 53(9):8127–8134. <https://doi.org/10.1002/2017WR020888>
 60. Wang JP, Gallo E, François B, Gabrieli F, Lambert P (2017b) Capillary force and rupture of funicular liquid bridges between three spherical bodies. *Powder Technol* 305:89–98. <https://doi.org/10.1016/j.powtec.2016.09.060>
 61. Wang JP, Hu N, François B, Lambert P (2017c) Estimating water retention curves and strength properties of unsaturated sandy soils from basic soil gradation parameters. *Water Resour Res* 53(7):6069–6088. <https://doi.org/10.1002/2017WR020411>
 62. Wang JP, Li X, Yu HS (2017d) Stress–force–fabric relationship for unsaturated granular materials in pendular states. *J Eng Mech* 143(9):04017068. [https://doi.org/10.1061/\(ASCE\)EM.1943-7889.0001283](https://doi.org/10.1061/(ASCE)EM.1943-7889.0001283)
 63. Yang H, Rahardjo H, Leong EC, Fredlund DG (2004) Factors affecting drying and wetting soil-water characteristic curves of sandy soils. *Can Geotech J* 41(5):908–920. <https://doi.org/10.1139/04-042>